Ambient Noise Rayleigh Wave Tomography Across Europe

Yingjie Yang, Michael H. Ritzwoller, Anatoli L. Levshin,
Center for Imaging the Earth's Interior
Department of Physics
University of Colorado at Boulder,
Boulder, CO 80309-0390 USA,
yingjie.yang@colorado.edu

and

Nikolai M. Shapiro
Laboratoire de Sismologie, CNRS
IPGP, 4 place Jussieu
75005 Paris, France

Submitted to Geophysical Journal International

June 19, 2006

Summary

We extend ambient noise surface wave tomography both in band-width (10 sec - 50 sec period) and geographical extent (across much of Europe) compared with previous applications. Twelve-months of ambient noise data from 2004 are analyzed. The data are recorded at about 125 broad-band seismic stations from the Global Seismic Network (GSN) and the Orfeus Virtual European Broad-band seismic Network (VEBSN). Cross-correlations are computed in daily segments, stacked over one-year, and Rayleigh wave group disperson curves from 8 sec – 50 sec period are measured using a phase-matched filter, frequency-time analysis technique. We estimate measurement uncertainties using the seasonal variation of the dispersion curves revealed in three-month stacks. On average, uncertainties in group delays increase with period from ~3 sec to ~ 7 sec from periods of 10 sec - 50 sec, respectively. Group speed maps at periods from 10 sec to 50 sec are estimated. The resulting path coverage is denser and displays a more uniform azimuthal distribution than from earthquake-emitted surface waves. The fit of the group speed maps to the ambient noise data is significantly improved below 30 sec compared to the fit achieved with earthquake data. Average resolution is estimated to be about 100 km at 10 sec period, but degrades with increasing period and toward the periphery of the study region. The resulting ambient noise group speed maps demonstrate significant agreement with known geologic and tectonic features. In particular, the signatures of sedimentary basins and crustal thickness are revealed clearly in the maps. These results are evidence that surface wave tomography based on cross-correlations of long time-series of ambient noise data can be achieved over a broad period band on nearly a continental scale and yield higher resolution and more reliable group speed maps than based on traditional earthquake-based measurements.

1. Introduction

Traditional inference of seismic wave speeds in Earth's interior is based on observations of waves emitted by earthquakes or human-made explosions. In the past decades, with the deployment of a large number of high-quality broad-band seismic stations across the globe, there have been numerous tomographic studies performed on both global and regional scales using the travel times of body waves, dispersion curves of surface waves, and waveform fitting methods. Much information has been obtained about the structure of Earth's interior using these methods.

Surface wave tomography has proven particularly useful in imaging Earth's crust and uppermost mantle on both regional and global scales. Because they propagate in a region directly beneath Earth's surface, surface waves typically generate better path coverage of the upper regions of Earth than body waves with the same distribution of seismic stations. Surface waves at different periods are sensitive to Earth structure at different depths, with the longer period waves exhibiting sensitivity to greater depths. By measuring the dispersive character of surface waves, the structure of the crust and upper mantle can be relatively well constrained. In Europe, many traditional surface wave studies have been performed in the past, both at regional (e.g., Papazachos, 1969; Nolet, 1977; Mueller and Sprecher, 1978; Maupin and Cara, 1992; Stange and Friederich, 1993; Vaccari and Panza, 1993; Pedersen et al., 1994; Lomax and Snieder, 1995; Pontevivo and Panza, 2002) and continental scales (e.g., Panza et al., 1980; Patton, 1980; Snieder, 1988; Marquering and Sneider, 1996; Ritzwoller and Levshin, 1998; Yanovskaya et al., 2000; Pasyanos, 2002; Pasyanos and Walter, 2002).

There are, however, basic limitations to earthquake-based surface wave tomography independent of the number of broad-band stations available. First, due to the uneven distribution of earthquakes around the world, seismic surface waves only sample certain preferential azimuths. In addition, in aseismic regions surface wave dispersion can be measured only from distant earthquakes. Second, it is difficult to obtain high-quality

short-period (<20 sec) dispersion measurements from teleseismic events due to intrinsic attenuation and scattering along ray paths. It is, however, the short-period waves that are most useful to constrain the structure of the crust and uppermost mantle. Third, inversions of seismic surface waves require some information about sources, such as earthquake hypocentral locations and moment tensors in some cases, that have a substantial intrinsic inaccuracy, particularly for small events.

Some of the problems that beset traditional earthquake surface wave tomography can be alleviated by observations made on diffuse wavefields (e.g., ambient noise, scattered coda waves). Theoretical research has shown that, under the right circumstances, the time-derivative of the cross-correlation of records from two seismic stations provides an estimate of the Green function between the stations, modulated by the spectrum of the noise source (Weaver and Lobkis, 2001a, 2001b, 2004; Derode et al., 2003; Snieder, 2004; Wapenaar, 2004; Larose et al., 2005). Seismic observations have confirmed the theory using both coda waves (Campillo and Paul, 2003; Paul et al., 2005) and ambient noise for surface waves (Shapiro and Campillo, 2004; Sabra et al., 2005a) and crustal body waves (Roux et al., 2005). Oceanic applications also appear to be feasible (Lin et al., 2006). The method has been successfully applied to stations in Southern California to obtain high-resolution surface wave tomography maps at short periods ranging from 7.5 to 15 sec (Shapiro et al., 2005; Sabra et al., 2005b). The group velocity maps from these studies show a striking correlation with geological units in California with low-speed anomalies corresponding to the principal sedimentary basins and high-speed anomalies corresponding to the igneous cores of the major mountain ranges. More recent applications have arisen across all of California and the Pacific Northwest while tracking the growth of the Transportable Array component of EarthScope (Moschetti et al., 2005), in South Korea at very short periods (Cho et al., 2006), in Tibet (Yao et al., 2006), and elsewhere in the world.

This research has shown, therefore, that information about Earth structure between a

pair of seismic stations can be extracted by cross-correlating long time sequences of seismic noise. With sufficient station density, cross-correlations of ambient seismic noise promise to yield more homogenous sampling over study regions than earthquakes, to provide information to shorter periods so as to improve constraints on crustal structure, and partially to release seismologists from the dependence on earthquakes in surface wave tomography.

The purpose of this paper is to determine whether ambient noise Rayleigh wave tomography can be applied reliably on a nearly continental scale and extended to intermediate periods up to ~50 sec. The study is based on data across Europe from 125 broad-band seismic stations from the Global Seismic Network (GSN) and the Virtual European Broad-band Seismic Network (VEBSN). We compute broad-band cross-correlations to produce estimated Green functions for all station-pairs using one-year time-series. The assessment of the reliability of the measurements is based on four primary criteria: (1) signal-to-noise ratio (SNR) of the cross-correlations, (2) seasonal repeatability of the dispersion measurements, which is the basis for the error analysis, (3) misfit of the measurements determined from tomography, and (4) consistency of the estimated group speed maps with known structural features such as sedimentary basins and crustal roots beneath mountain ranges. Group velocity curves across Europe are measured from 10 to 50 sec period and we present group speed maps from 10 to 40 sec period. The results are compared, whenever possible, to earthquake-based measurements and maps produced earlier by the University of Colorado at Boulder (CU-B) in order to quantify the relative merits of ambient noise and earthquake tomography.

2. Data processing and group velocity measurements

Europe is an excellent region to test ambient noise surface wave tomography. Broad-band seismic station coverage is dense across much of the continent and the

substantial a priori knowledge of geological structures allows us to evaluate the reliability of the resulting group velocity maps. We have collected continuous vertical-component seismic data from 125 stations including data from the Global Seismic Network (GSN) and the Virtual European Broad-Band Seismic Network (VEBSN) (Figure 1) over the 12 months of 2004. About 110 of these stations returned useful data.

The data processing procedure that is applied here is very similar to that discussed at greater length in the paper by Bensen et al. (2006). Using vertical-component seismic data implies that the resulting cross-correlations contain only Rayleigh wave signals. Data are processed one day at a time for each station after being decimated to 1 sample per second and are band-pass filtered in the period band from 5 to 150 sec after the daily trend, the mean and the instrument response are removed. Data are then normalized in time and whitened over the frequency-band of interest prior to cross-correlation. Spectral whitening is a straightforward procedure, but the temporal normalization requires more discussion.

Temporal normalization is a general phrase that describes a variety of methods used to remove earthquake signals and instrumental irregularities from the time-series prior to cross-correlation. At periods where earthquake signals are stronger than ambient noise, roughly above about 20 sec period, some method of removing earthquake signals is imperative. For this purpose, Shapiro et al. (2005) used one-bit normalization, which generates a data stream composed only of the values 1 and -1, retaining only the sign and disregarding the amplitude of the signal completely (Larose et al., 2004). Other researchers have used different methods; for example, Sabra et al. (2005b) used a truncation threshold for each station to clip seismograms. Based on observations of the signal-to-noise ratio of the cross-correlations, we have come to prefer applying a weighted running average on the envelope of each seismogram in the time domain, which effectively removes earthquake signals while keeping much of the information on the amplitude of the ambient noise. The process applied here computes the average of the

envelope of the seismogram over a normalization time interval, and weights the seismogram by the inverse of this average at the center of the window. The width of the normalization window determines how much amplitude information is retained. A one-sec window is equivalent to one-bit normalization; while an infinitely long window is equivalent to the original signal. After testing various time windows, we find that a time window with width equal to half the maximum period of the band-pass filter works well. The maximum period here is 150 sec, so the normalization window is about 75 sec in duration. Normalization windows from 50 to 100 sec in duration produce nearly indistinguishable results. This procedure temporal normalization is found to generate a somewhat higher SNR than 1-bit normalization, on average. In addition, the procedure is more flexible, allowing, for example, the computation of the temporal weights in a sub-band (e.g., 15 – 50 sec designed to remove earthquakes) but with application to the broad-band signal.

After the time-series has been processed for each day, we then compute daily cross-correlations in the period band from 5 to 150 sec between all station-pairs and then stack the results into a set of three-month and one-year time series. The stacking simply involves adding the daily cross-correlations without weights if the time series covers more than 80% of the day, otherwise the day of data is discarded. For the year of data, 12 three-month stacks are produced starting at each month; namely, months 1, 2, 3; months 2, 3, 4; … ; months 11, 12, 1; and months 12, 1, 2. The three-month stacks are used to investigate the seasonal variability of the measurements, which is the basis for the error analysis and is part of the data selection procedure discussed further below.

The resulting cross-correlations contain surface wave signals coming from opposite directions along the path linking the stations. These two signals appear at positive and negative correlation lag and are sometimes called the “causal” and “acausal signals”. Although the two signals sample the same structure between a station pair, the source characteristics in the two directions may be very different, so the spectral content of the

cross-correlations may differ appreciably. Asymmetric cross-correlations are, in fact, common. To simplify data analysis and enhance the signal-to-noise ratio (SNR), we separate each cross-correlation into positive and negative lag components and then average these two components to form a final cross-correlation, which we call the "symmetric component". The following analysis is done on the symmetric components exclusively.

An example of a broad-band (5 to 150 sec) symmetric-component cross-correlation for the station pair IBBN and TIRR is shown in Figure 2 together with the cross-correlation filtered into five frequency sub-bands. Rayleigh waves emerge clearly in each frequency band with the earlier arriving waves being at longer periods. In Figure 3, we plot an example of a cross-correlation record-section with the central station being TUE. This figure shows that a variety of azimuths produce visible signals, but not all azimuths are covered for every station. Good azimuthal path coverage is important to improve resolution and reduce smearing effects in surface wave tomography.

To begin to evaluate the quality of the cross-correlations quantitatively, we calculate the signal-to-noise ratio (SNR) for each cross-correlation. SNR is defined as the ratio of the peak amplitude within a time window containing the signals to the root-mean-square of noise trailing the signal arrival window. The signal window is determined using the arrival times of Rayleigh waves at the minimum and maximum periods of the chosen pass-band. The group velocities used to predict arrival times here are calculated from the global 3-D shear velocity model of Shapiro and Ritzwoller (2002). Because the SNR can vary strongly with frequency, we filter the broad-band cross-correlations in three narrower pass-bands at 8-25 sec, 20-50 sec and 33-70 sec and compute the SNR in each band. We reject cross-correlations with SNR less than 7 in each band. This value is chosen as a compromise between optimizing measurement quality and quantity. We identify the cross-correlations with SNR > 7 as the estimated Green functions. The data selection criteria are significantly more complicated than this, and are described in

section 3. Group velocity curves are measured on the estimated Green functions that emerge from both the three-month and one-year stacks in each of the three period bands using automatic Frequency Time Analysis (FTAN) as described in the next paragraph.

As in earthquake dispersion analysis (e.g., Ritzwoller and Levshin, 1998), our automated dispersion measurement is based on Frequency Time Analysis (FTAN) in a two-step process. Bensen et al. (2006) discuss this procedure in greater detail, but here we provide a brief overview. In the first step, traditional FTAN creates a two-dimensional diagram of signal power as a function of time and the central frequency of the applied filters (Fig. 4, middle). The automatic procedure tracks the local power maximum along the frequency axis. The group arrival times of the maximum amplitude as a function of filter frequency are used to calculate the tentative (raw) group velocity curve. Measures are taken to ensure the continuity of this curve by rejecting jumps in group arrival times. Formal criteria are set to reject curves with distinctly irregular behavior or to interpolate through small spectral holes by selecting realistic local instead of absolute maxima. The second part of the method is the application of a phase-matched or anti-dispersion filter (Fig. 4, bottom). In the non-automated method that has been applied to large numbers of earthquake signals (e.g., Ritzwoller and Levshin, 1998), the analyst defines both the phase-matched filter and the frequency band of the measurement. In the automated method that we use here, the frequency band of measurement is pre-set and the phase-matched filter is defined by the dispersion curve that results from the first step of the process. Phase-matched filtering collapses the signal into a "delta-like" arrival, ideally. In the traditional analysis, the analyst defines a window to extract this signal, which is then redispersed and a cleaned FTAN image is returned (Fig. 4, bottom). The automated procedure is similar, but the windowing and extraction of the signal is done automatically. In both the traditional and automated analyses, the actual frequency of a given filter is found from the phase derivative of the output at the group time of the selected amplitude maximum (Levshin and Ritzwoller, 2001). Figure 4 shows an

example of the FTAN procedure for the cross-correlation between 12-month time series from station IBBN and station TUE. Bensen et al. (2006) also discuss the method to measure phase velocities, but only group velocities are used in the present paper.

3. Data selection and uncertainty estimation

The automated measurement procedure must be followed by the application of criteria to select the data. We apply three general types of criteria: (1) signal-to-noise ratio (SNR), (2) repeatability of the measurements (particularly seasonal variability), and (3) coherence across the set of measurements. The formal uncertainty analysis is based on seasonal variability.

First, we reject a cross-correlation if its SNR < 7. (The definition of SNR is presented in section 2.) Figure 5a shows an example histogram of the distribution of SNR for signals band-pass filtered between 20 and 50 sec. Distributions are similar in the other two pass-bands, between 8 and 25 sec and between 33 and 70 sec. The mode of the distribution is less than a SNR of 5, and the SNR cut-off of 7 eliminates about half the measurements, as Figure 5b shows. The jump between the two levels seen in Figure 5b is caused by lower SNR in the pass-band from 25 to 50 sec than in the band between 5 sec and 25 sec period. Although we have found that it is often possible to obtain high quality dispersion measurements on waveforms with SNR less than 7, such measurements are frequently erroneous and in an automated procedure it is best to reject them.

Second, for a measurement to be accepted, it needs to be repeatable in the sense that measurements obtained at different times should be similar. This is not a trivial constraint, because both the spectrum and the directional-dependence of ambient noise vary strongly with season. The repeatability of measurements obtained on different time intervals, in particular in different seasons, is, in addition to a data selection criterion, the basis for our formal assessment of measurement uncertainties. For surface waves that are emitted from

earthquakes, it is difficult to estimate uncertainties in the group velocity measurements. Only when several earthquakes occur near to the same location or when waves follow nearly the same path connecting two stations can uncertainties be estimated. These criteria are not achieved for the vast majority of earthquake measurements, so only average error statistics can be estimated for earthquakes. In contrast, dispersion measurements from cross-correlations of ambient noise are naturally repetitive.

The repeatability criterion is based on quantifying seasonal variability. To do so, we select 12 over-lapping three-month time-series for each station-pair. The three-month time windows capture the seasonal variation of dispersion measurement, but are also long enough to obtain reliable dispersion measurements in many (but not all) cases. Figure 6 shows an example of the seasonal variability in the observed dispersion curves. The variability typically increases with period, partially due to the fact that the amplitude of ambient noise decreases above 20 sec period but also because ambient noise above the microseism band appears to be less azimuthally homogenous. Thus, the longer period signals are more likely to be contaminated by precursory noise that results from incomplete destructive interference of the signals that are off the azimuth between the stations.

The dispersion curves that are used for tomography here are taken from the 12-month stacks. The standard deviation is computed for a station-pair if more than 4 three-month stacks have a SNR > 7. The measurement is retained if the standard deviation is less than 100 m/sec. It is rejected if the standard deviation either cannot be computed due to the fact that too few measurements can be obtained on the 3-month stacks or if the standard deviation is too large. The effect of this step in eliminating measurements is shown in Figure 5b. Equating the seasonal variability with the measurement uncertainty is probably a conservative error estimate. Repeated biased measurements, however, could bias the uncertainty low. Such repetition is unlikely due to the fact that the sources of ambient noise change significantly with season in azimuth,

amplitude, and spectral content.

Figures 5d and 5e show the average measurement uncertainties taken over the entire European data set. Average uncertainties of group velocities and group arrival times increase with period from ~0.02 km/s or ~ 3 sec at 10 sec period to 0.09 km/s or 7.5 sec at 50 sec period. Compared to uncertainties of group velocities of earthquake data using cluster analysis by Ritzwoller and Levshin (1998), we find that our group velocity uncertainties tend to be smaller at periods shorter than 20 sec and larger at periods longer than 30 sec. The reason for larger uncertainties at periods longer than 30 sec is due to the shorter average path length in our data set, which is about 1200 km (Fig. 5c) compared to more than 4000 km in Ritzwoller and Levshin. The uncertainties in group arrival times are much smaller in this study, however. The travel time uncertainties average less than 20% of a period. This is still a substantial error, attributable largely to the fact that the average SNR of the retained measurements remains fairly low. The SNR of earthquake data tends to be larger, but earthquake measurements are affected by uncertainties in source characteristics that provide a lower bound for measurement errors.

Third, we require that the measurements cohere with one another across the data set. Incoherent measurements that disagree with other measurements in the data set are identified during tomography. This is discussed further in section 5.

Finally, we find that to obtain a reliable measurement, the stations must be separated by at least 3 wavelengths. Each dispersion curve is retained only up to a period equal to one-third of the observed travel-time. For a phase velocity of 4 km/sec, for example, this implies that if a station-pair is separated by a distance Δ in km, a dispersion curve is accepted only up to a maximum cut-off period of $\Delta/12$ in seconds. In practice, this criterion has only limited practical effect because short-path measurements tend to be eliminated by the previous criteria.

The number of measurements that remain after all criteria have been applied is shown in Figure 5b. Less than a third of the original measurements are retained for

tomography. The least satisfying part of the procedure is eliminating what appears to be a good measurement on the 12-month stack because the uncertainty estimate could not be determined, usually because of an insufficient number of high SNR 3-month stacks. To retain a higher percentage of measurements, it would probably be necessary to process two or more years of data. This would increase the SNRs of the seasonal stacks and be preferable over a single year of data. Bensen et al. (2006) discuss this further.

4. Method of surface wave tomography

The dispersion measurements of Rayleigh waves from one-year cross-correlations are used to invert for group velocity maps on a $1^o \times 1^o$ grid across Europe using the tomographic method of Barmin et al. (2001). This method is based on minimizing a penalty function composed of a linear combination of data misfit, model smoothness and the perturbation **m** to a reference model $\mathbf{m}_o$ for isotropic wave speed:

$$(Gm-d)^T C^{-1}(Gm-d)+\alpha^2\|F(m)\|^2+\beta^2\|H(m)\|^2 \qquad (1)$$

where **G** is the forward operator that computes travel times from a map; **d** is the data vector whose components are the observed travel time residuals relative to the reference map; **C** is the data covariance matrix or matrix of data weights whose elements are determined from standard deviations of the dispersion measurements based on seasonal variability; **F** is a Gaussian spatial smoothing operator; and **H** is an operator that penalizes the norm of the model in regions with poor path coverage. The result of **H** is to blend smoothly the estimated map **m** into the reference map $\mathbf{m}_o$ where data coverage is low. If an input reference map in not given, then the average of the measurements specify $\mathbf{m_0}$. The spatial smoothing operator **F(m)** is defined over a 2-D tomographic map as follows:

$$F(m)=m(r)-\int_S S(r,r')m(r')dr' \qquad (2)$$

where *S* is a smoothing kernel defined as below:

$$S(r,r') = K_0 \exp\left(-\frac{|r-r'|^2}{2\sigma^2}\right), \quad (3)$$

$$\int_S S(r,r')dr' = 1, \quad (4)$$

σ is the spatial smoothing width or correlation length and the vector **r** is a position vector on Earth's surface. A more detailed discussion of this method is given by Barmin et al. (2001).

The choice of the damping parameters α and β and the smoothing width σ is subjective. We perform a series of tests using different combinations of these parameters to determine acceptable values by considering data misfit, model resolution, and model norm. Ray theory is used to compute the travel times of surface waves. In recent years, surface wave studies have increasing moved toward diffraction tomography using spatially extended finite-frequency sensitivity kernels based on the Born/Rytov approximation (e.g. Clevede et al. 2000; Spetzler et al., 2002; Ritzwoller et al., 2002; Yoshizawa & Kennett, 2002, Zhou et al., 2004; many others). Ritzwoller et al. (2002) showed that diffraction tomography recovers similar structure to ray theory at periods shorter than 50 sec in most continental regions. In the context of regional tomography with dense path coverage, Sieminski et al. (2004) showed that nearly identical resolution can be achieved using ray theory as that using finite-frequency theory. In this study, we concentrate on Europe where station coverage and the resulting ray paths are both dense, so that ray theory suffices for surface wave tomography.

Resolution is estimated using the method described by Barmin et al. (2001) with modifications presented by Levshin et al. (2005). Each row of the resolution matrix is a resolution surface (or kernel), which is a map defining the resolution at one spatial node. Information in the resolution surface is summarized by a single scalar quantity at each node, called the spatial resolution. Because the shape of the resolution surface for most nodes resembles a 2-D spatial Gaussian function, we fit a 2-D symmetric spatial Gaussian function to the surface at each node:

$$A\exp\left(-\frac{|r|^2}{2\gamma^2}\right). \qquad (5)$$

The spatial resolution at each node is summarized by the standard deviation γ parameter of the best-fit Gaussian function to the resolution map.

5. Group speed maps

Group speed tomography is performed in two steps. The first, preliminary, step generates overly smoothed maps at each period in order to identify and reject any remaining bad measurements. The over-smoothed model fits most data well as the example misfit histogram for the 16 sec data set shows in Figure 7a. We discard group velocity measurements with travel time residuals larger than 15 sec, which is about the RMS value of the travel time residuals at most periods. The number of paths remaining after data reduction is listed in Figure 5bb. Although there are about 5800 inter-station paths, after data rejection only about 20-30% off paths remain.

The second step of tomography is the construction of the final maps. Maps are constructed on a 1^o x 1^o grid across Europe and are defined relative to the reference maps computed from the 3-D model of Shapiro and Ritzwoller (2002). In an important sense, the reference maps already have a priori information imposed on crustal structure. The 3-D model itself was constructed as a perturbation to a starting model

that included information about sediments and crustal thicknesses. For this reason, we choose to seek only smooth perturbations to the reference maps.

Examples of path density and resolution are shown in Figure 8 for the 16 sec measurements. Results are similar from 10 sec to 50 sec period, although there is a reduction in path density and resolution with increasing period due to the decrease in the number of measurements at long periods. The resolution of surface wave tomography depends primarily on path density and the azimuthal distribution of paths. The azimuthal distribution of paths is good in the center of the study region as demonstrated by Figure 3, but deteriorates near the boundaries. Path density is highest in the center of Europe and also gradually degrades toward the edge of the study region. As Figure 8 indicates, average resolution is estimated to be about 100 km in the center of the study region in Europe, and degrades toward the periphery of the map where station coverage is minimal.

The results of group velocity tomography at 10, 16, 20, 30, 35, and 40 sec periods are shown in Figures 9, 10a, and 11a. In the inversion, reference group velocity maps predicted from the global 3-D shear velocity model of Shapiro and Ritzwoller (2002) are used as starting models. Examples of the reference maps are shown in Figure 12 at 16 sec and 35 sec period. Figures 10b and 11b illustrate that the perturbations introduced during tomography are smooth and occur only in regions where path coverage is high, predominantly in the center of the region of study. In most of the Mediterranean Sea, the Atlantic Ocean, North Africa, the Iberian Peninsula, and far eastern Europe, the perturbations are small and the estimated maps are very similar to the reference maps. The features of the maps are observed to vary gradually with period due to the overlapping depth ranges of Rayleigh wave depth-sensitivity. Many of the observed anomalies are correlated with known geological units, which is discussed further in section 6.

Figure 13a shows the improvement in fit to the measured dispersion curves achieved by the resulting group velocity maps, expressed as the variance reduction relative to the predicted group velocity maps. In addition, variance reduction relative to the average across each map is shown. Variance reductions relative to predicted group velocity (solid line) are larger at short periods (< 25 sec) and smaller at long periods (>35 sec) than relative to the average (dashed line). Variance reductions are highest at short periods and gradually decrease with period. The observed trend of variance reductions because group speed anomalies are largest at short periods and also the 3-D model is more reliable for the longer periods. In particular, Figure 10b shows that below about 20 sec period the average of the reference model is too high. Only periods above about 20 sec went into the construction of the 3-D model of Shapiro and Ritzwoller (2002). The RMS group velocity and travel time misfits after tomography are also shown in Figures 13b and 13c. Travel time misfit of the final data set is ~5 - 6 sec and is nearly independent of period. Contrast this with the mean uncertainty that trends from ~2 sec to 7 sec shown in Figure 5e. Most of the misfit at long periods, therefore, is probably due to measurement error. At short periods, however, about half of the misfit has another cause, perhaps being due to unspecified structures such as azimuthal anisotropy or smaller scale structures.

6. Discussion

The principal purpose of this paper is to assess the reliability of ambient noise tomography applied to large regions, such as Europe, across a broad frequency band that extends from short to intermediate periods. We base our assessment on several lines of evidence: (1) the repeatability of the measurements, (2) the coherence of the measurements with one another, and (3) the agreement of the resulting group speed maps with known geological structures. The first two of these criteria have already been invoked as part of the data selection procedure.

First, the repeatability of the measurements, particularly as they change with the variable ambient noise conditions in different seasons, is discussed above and is the basis for the estimates of measurement uncertainties. As discussed in section 5, a measurement is retained only if it is shown to be robust over multiple seasons. Not all measurements satisfy this criterion, but many do, as Figure 5b illustrates. This is the foundation for much of our confidence in the ambient noise dispersion measurements.

Second, the "coherence" of the measurements relates to the mutual agreement of measurements that cross the same region. This can be determined from the ability to fit the data with smooth tomographic maps, particularly as that fit compares to that achieved with earthquake data. Figure 7 plots example histograms of tomographic misfit from over-smooth maps using ambient noise and earthquake data in Europe measured at CU-B. The ambient noise data are fit better, partially due to the fact that earthquake data possess sensitivity to uncertainties in source characteristics. Figure 14 summarizes the standard deviation of tomographic misfit for both earthquake and ambient noise data across Europe using the over-smooth maps. These results are taken prior to the last stage in data rejection; the rejection due to tomographic misfit. This is in contrast to Figure 13c, which is misfit after data selection is completed. Figure 13c, therefore, has a lower misfit level. As periods reduce below 30 sec in Figure 14, relative misfit of ambient noise improves, particularly below about 15 sec period. We take this as evidence that short-period dispersion measurements (<20 sec) obtained from ambient noise typically are preferable to earthquake derived measurements.

The final criterion to assess the credibility of the estimated maps is agreement with known geological structures. Although the best test may be to interpret a 3-D model constructed from the group speed maps, to address the question more simply one can exploit how surface waves at different periods are sensitive to Earth structure over different depth ranges. The depth of maximum sensitivity is about one-third of a wavelength. At the short-period end of this study (10-20 sec), group velocities are

dominantly sensitive to shear velocities in the upper crust. Because the seismic velocities of sediments are very low, short-period low velocity anomalies are a good indicator of sedimentary basins. At the intermediate periods of this study (25-35 sec), Rayleigh waves are primarily sensitive to crustal thickness and the shear velocities in the lower crust and uppermost mantle. Due to the large velocity contrasts across the Moho, the group velocities in this band should vary approximately inversely with crustal thickness, with high velocities in regions with a thin crust and low velocities regions with a thick crust.

To aid assessment, Figure 15 presents a map of sediment thickness from CRUST1.0, which Laske and Masters digitized across most of Europe from the EXXON Tectonic Map of the World (Laske and Masters, 1997), and a map of crustal thickness taken from CRUST2.0 (Bassin, et al., 2000). We identify the names of several geological units on these maps, mainly sedimentary basins and mountain ranges.

Comparison of the estimated group speed maps with known geological structures is the thorniest of the assessment tests, both because understanding of known structures is imperfect but more pointedly because a priori information has already been imparted to the reference maps (derived from the 3-D model of Shapiro and Ritzwoller, 2002)) that form the basis for tomography. In fact, the reference model does not strongly affect the estimated group speed maps in areas of high data coverage. To demonstrate this, Figures 10c and 11c present maps constructed with no input reference model. Comparison with Figures 10a and 11a establishes the point – in regions of high data coverage an estimated map can be compared with a priori knowledge without worry of contamination by information contained in the reference map. Figures 10d and 11d also show explicitly that the reference model imposes little constraint on the estimated map in areas of high data coverage.

The 10 sec and 16 sec group speed maps in Figures 9 and 10 exhibit low velocity anomalies associated with most of the known sedimentary basins across Europe. In regions of high data coverage, low-velocity anomalies are observed in the North Sea

Basin, the Silesian Basin (North Germany, Poland), the Pannonian Basin (Hungary, Slovakia), the Po Basin (North Italy), the Rhone Basin (Southern France), and the Adriatic Sea. Not surprisingly, many of these features already exist in the reference map. Because there is little resolution in the Mediterranean and Black Seas, as Figure 8 shows, the basins there are imposed by the reference model. The new features recovered from ambient noise tomography below 20 sec period are (1) a general reduction of group speeds in the center of the region of study, (2) generation of a much more pronounced low velocity anomaly associated with the Po and Pannonian Basins, and (3) increase in group speeds directly north of the Hellenic Arc. In particular, the low velocity anomaly observed in the Pannonian Basin is stronger than expected from the Exxon sediment maps, which estimates the sediments to be about 2 km thick. A recent study by Grad et al. (2006) includes a 2-D tomographic model, constructed from a refraction profile running from the East European craton to the Pannonian Basin. In this model, the sediments of the Pannonian Basin extend to a depth of ~5 km, which is more consistent with our observed 5-10% lower group velocities in this region.

At intermediate periods (25 to 40 sec), group velocities are quite sensitive to crustal thicknesses. These estimated maps exhibit low-velocity anomalies associated with the Alps, the Carpathians and the mountains in the Balkan region. The low velocity anomalies are probably caused by deeper crustal roots beneath mountain regions which occur due to isostatic compensation. The general reduction in Rayleigh wave velocity in the eastern part of the 30 - 40 sec maps in Figures 9 and 11 is probably related to the general thickening of the crust toward the east European craton, where the crust is about 45 km thick (Grad et al., 2006).

More detailed interpretation of the observed anomalies is beyond the scope of this work, and awaits complementary research, which will include inversion for the *Vs* structure of the crust and upper mantle in Europe. The group velocity maps of our study, particularly at periods below ~20 sec, provide unique constraints on crustal thickness and

shear wave velocities in the crust and uppermost mantle.

7. Conclusions

In this study, we use ambient noise data recorded at 125 broad-band seismic stations available from the Global Seismic Network (GSN) and the Orfeus Virtual European Broad-band seismic Network (VEBSN). Cross-correlations are computed in abroad period band from 5 sec to 150 sec in daily segments with a duration of one-year. Rayleigh wave group velocities for station-pairs are measured from one-year stacks of daily cross-correlations using a phase-match filtering frequency-time analysis procedure. Uncertainties of the group velocities are estimated based on seasonal variations of the dispersion curves using three-month time-series. An automated data selection procedure is applied to all dispersion measurements using signal-to-noise ratio and seasonal repeatability as selection criteria. About 20–30% of all station-station cross-correlations are retained for surface wave tomography after data rejection. All measurements have uncertainty estimates that derive from observations of seasonal variability. The data set would benefit from time-series of 2 or more years, which would allow most uncertainties to be measured and, therefore, more measurements will pass the selection criterion.

Group velocity maps at periods from 10 sec to 50 sec are obtained using ambient noise tomography. These maps provide a significant improvement in the understanding of surface wave dispersion in Europe, particularly at periods below about 20 sec. This study has a denser and more uniform data coverage and demonstrates higher resolution than pervious studies which have relied on traditional earthquake-based surface wave tomography. Estimated resolution is ~100 km at 10 sec period, but degrades slowly with period above above 25 sec. Tomographic misfit of group speeds measured from ambient noise shows a significant improvement over earthquake based measurements below 30 sec period, particularly below 15 sec. The group velocity maps agree well with known geologic features, such as sedimentary basins and the lateral variation of crustal thickness.

Observations at short periods (10 - 20 sec) provide entirely new constraints on sediment thickness, crustal thickness, and the shear velocity structure of crust.

In summary, this study demonstrates that surface wave tomography based on cross-correlations of long time-series of ambient noise data can be achieved over a broad period band on a nearly continental scale and yield higher resolution and more reliable group velocity maps than based on traditional earthquake-based measurements.

Acknowledgments

All of the data used in this research were downloaded from the continuous ftp database of the Orfeus (Observatories and Research Facilities for European Seismology) Data Center and from the IRIS Data Management Center. In particular, the authors are deeply grateful to the data contributors to the Virtual European Broadband Seismic Network (VEBSN), a partnership of more than 30 local, regional and global arrays and network. The list of contributors is located at **http://www.orfeus-eu.org/meredian/vebsn-contributors.htm**. This research was supported by a contract from the US Department of Energy, DE-FC52-2005NA26607.

References

Barmin, M.P., M.H. Ritzwoller, and A.L. Levshin, 2001. A fast and reliable method for surface wave tomography, *Pure Appl. Geophys.*, **158**, 1351 - 1375.

Bassin, C., Laske, G. and Masters, G., 2000. The current limits of resolution for surface wave tomography in North America, *EOS Trans AGU*, **81**, F897.

Bensen, G.D., M.H. Ritzwoller, N.M. Shapiro, A.L. Levshin, 2005. Extending ambient noise surface wave tomography to continental scales: Application across the United States, *EOS Trans. AGU*, **86**(52), Fall Meeting Suppl., Abstract S31A-0274.

Bensen, G.D., M.P. Barmin, F.-C. Lin, M.P. Moschetti, Y. Yang, A.L. Levshin, N.M.Shapiro, and M.H. Ritzwoller, 2006. Obtaining robust group and phase speed curves for ambient noise tomography, manuscript in preparation.

Cho, K.H., R.B. Hermann, C.J. Ammon, and K. Lee, 2006. Imaging the upper crust of the Korean Peninsula by surface-wave tomography, *Bull. Seism. Soc, Amer.,* submitted.

Campillo M. and A. Paul, 2003. Long-range correlations in the diffuse seismic coda, *Science*, **299**,547-549.

Clevede, E., Megnin, C., Romanowicz, B. & Lognonne, P., 2000. Seismic waveform modeling and surface wave tomography in a three-dimensional Earth: asymptotic and non-asymptotic approaches, *Phys. Earth Planet. Int.*, **119**,37-56.

Derode, A., E. Larose, M. Tanter, J. de Rosny, A. Tourim, M. Campillo, and M .Fink, 2003. Recovering the Green's function from filed-field correlations in an open scattering medium (L), *J. Acoust. Soc. Am.*, **113**,2973-2976.

Grad, M., A. Guterch, G. R. Keller, T. Janik, E. Hegedűs, J. Vozár, A. Ślączka, T. Tiira, and J. Yliniemi, 2006. Lithospheric structure beneath trans-Carpathian transect from Precambrian platform to Pannonian basin: CELEBRATION 2000 seismic profile CEL05, *J. Geophys. Res.,* **111**, B03301, doi:10.1029/2005JB003647.

Larose, E., A. Derode, M. Campillo, and M. Fink, 2004. Imaging from one-bit correlations of wideband diffuse wavefields, *J. Appl. Phys*., **95**, 8393-8399.

Larose, E., A. Derode, D. Corennec, L. Margerin, and M. Campillo, 2005. Passive retrieval of Rayleigh waves in disoredered elastic media, *Phys. Rev. E.*, **72**, 046607, doi:10.113/PhysRevE.72.046607.

Laske, G. and G. Masters, 1997. A Global Digital Map of Sediment Thickness, *EOS Trans. AGU*, **78**, F483.

Levshin, A.L. and M.H. Ritzwoller, 2001. Automated detection, extraction, and measurement of regional surface waves, *Pure Appl. Geophys.*, **158**, 1531-1545.

Levshin, A.L., M.P. Barmin, M.H. Ritzwoller, and J. Trampert, 2005. Minor-arc and

major-arc global surface wave diffraction tomography, *Phys. Earth Planet. Ints.*, **149**, 205-223.

Lin, F., M.H. Ritzwoller, and N.M. Shapiro, Is ambient noise tomography acrosss ocean basins possible?, *Geophys. Res. Lett.*, in press.

Lomax, A., and R. Snieder, 1995. The contrast in the upper mantle shear-wave velocity between the East European Platform and tectonic Europe obtained with genetic algorithm inversion of Rayleigh-wave group velocity dispersion, *Geophys. J. Int.*, **123**,169-182.

Marquering, H., and R. Snieder, 1996. Shear-wave velocity structure beneath Europe, the northeastern Atlantic western Asia from wavefrom inversions including surface-wave mode coupling, *Geophys. J. Int.*, **127**, 283-304.

Maupin, V., and M. Cara, 1992. Love-Rayleigh wave incompatibility and possible deep upper mantle anisotropy in the Iberian peninsula, *Pure Appl. Geophys.,* **138**(3), 429-444.

Mueller, S., and C. Sprecher, 1978. Upper mantle structure along a profile through the eastern Alps from Rayleigh wave dispersion, in *Alps, Apennines, Hellenides*, edited by H. Closs, *Int. Geodyn. Comm. Sci. Rep*., **38**, 40-44.

Nolet, G., 1977. The upper mantle under western Europe inferred form the dispersion of Rayleigh wave modes, *J. Geophys.*, **43**, 265-276.

Panza, G.F., Mueller, S., and Calcagnile, G., 1980. The gross features of the lithosphere-asthenosphere system in Europe from seismic surface waves and body waves, *Pure Appl. Geophys*., **118**, 1209-1213.

Papazachos, B.C., 1969. Phase velocities of Rayleigh waves in Southeastern Europe and Eastern Mediterranean Sea, *Pure Appl. Geophys*., **75**, 47-55.

Pontevivo, A., and Panza, G.F., 2002. Group velocity tomography and regionalization in Italy and bordering areas, *Phys. Earth Planet. Inter.*, **134**, 1-15.

Pasyanos, M.E., 2005. A variable resolution surface wave dispersion study of Eurasia,

North Africa, and surrounding regions, *J. Geophys. Res.*, **110**, B12301, doi: 10.1029/2005JB003749.

Pasyanos, M. E. and W. R. Walter, 2002. Crust and upper-mantle structure of North Africa, Europe and the Middle East from inversion of surface waves, *Geophys. J. Int.*, **149**,463-481.

Patton, H., 1980. Crustal and upper mantle structure of the Eurasian continent from the phase velocity and Q of surface wave, *Rev. Geophys.*, **18**,605-625.

Paul, A., M. Campillo, L. Margerin, E. Larose, and A. Derode, 2005. Empirical synthesis of time-asymmetrical Green functions from the correlation of coda waves, *J. Geophys. Res.*, **110**, B08302, doi:10.1029/2004JB003521.

Pedersen, H. A., M. Campillo, and N. Balling, 1994. Changes in the lithospheric structure across the Sorgenfrei-Tornquist Zone inferred from dispersion of Rayleigh waves, *Earth Planet. Sci. Lett.*, **128**,37-46.

Ritzwoller, M. H. and A. L. Levshin, 1998. Eurasian surface wave tomography: group velocities, *J. Geophys. Res.*, **103**, 4839-4878.

Ritzwoller, M.H., Shapiro, N.M., Barmin, M.P., & Levshin, A.L., 2002. Global surface wave diffraction tomography, *J. Geophys. Res.*, **107**, B12, 10.1029/2002JB001777.

Roux, P., K.G. Sabra, P. Gerstoft, W.A. Kuperman, and M.C. Fehler, 2005. P-waves from cross-correlation of seismic noise, *Geophys. Res. Lett.*, **32**, L19393, doi:10.1029/2005GL023803.

Sabra, K. G., P. Gerstoft, P. Roux, W. A. Kuperman, and M. C. Fehler 2005a. Extracting time-domain Green's function estimates from ambient seismic noise, *Geophys. Res. Lett.*, **32**, L03310, doi:10.1029/2004GL021862.

Sabra, K. G., P. Gerstoft, P. Roux, W. A. Kuperman, and M. C. Fehler 2005b. Surface wave tomography from microseism in southern California, *Geophys. Res. Lett.*, **32**, L14311, doi:10.1029/2005GL023155.

Shapiro, N.M. and M. Campillo, 2004. Emergence of broadband Rayleigh waves from

correlations of the ambient seismic noise, *Geophys. Res. Lett.*, **31**, L07614, doi:10.1029/2004GL019491.

Shapiro, N.M. and M.H. Ritzwoller, 2002. Monte-Carlo inversion for a global shear velocity model of the crust and upper mantle, *Geophys. J. Int.*, **151**, 88-105.

Shapiro, N.M. M. Campillo, L. Stehly, and M.H. Ritzwoller, 2005. High resolution surface wave tomography from ambient seismic noise, *Science*, **307**, 1615-1618.

Sieminski, A., J.-J. Leveque, and E. Debayle, 2004. Can finite-frequency effects be accounted for in ray theory surface wave tomography?, *Geophys. Res. Lett.,* **31**, L24614, doi:10.1029/2004GL021402.

Snieder, R., 1988. Large-Scale Waveform Inversions of Surface Waves for Lateral Heterogeneity, 2, Application to Surface Waves in Europe and the Mediterranean, *J. Geophys. Res.*, **93**, 12067-12080.

Snieder, R., 2004. Extracting the Green's function from the correlation of coda waves: A derivation based on stationary phase, *Phys. rev. E*, **69**, 046610.

Spetzler, J., Trampert, J. & Snieder, R., 2002. The effects of scattering in surface wave tomography, *Geophys. J. Int.*, **149**,755-767.

Stange, S., and W. Friederich, 1993. Surface wave dispersion and upper mantle structure beneath southern Germany from joined inversion of network recorded teleseismic events, *Geophys. Res. Lett.*, **20**, 2375-2378.

Vaccari, F., and G. F. Panza, 1993. Vp/Vs estimation in southwestern Europe from P-wave tomography and surface wave tomography analysis, *Phys. Earth Planet. Inter.*, **78**, 229-237.

Wapenaar, K., 2004. Retrieving the elastodynamic Green's function of an arbitrary inhomogeneous medium by cross correlation, *Phys. Rev. Lett.*, **93**, 254301, doi:10.1103/PhysRevLett.93.254301.

Weaver, R.L. and O. I. Lobkis, 2001a. Ultrasonics without a source: Thermal fluctuation correlation at MHZ frequencies, *Phys. Rev. Lett.*, **87**, paper 134301.

Weaver, R.L. and O.I. Lobkis, 2001b. On the emergence of the Green's function in the correlations of a diffuse field, *J. Acoust. Soc. Am.*, **110**, 3011-3017.

Weaver, R.L. and O.I. Lobkis, 2004. Diffuse fields in open systems and the emergence of the Green's function, J. Acoust. Soc. Am., 116, 2731-2734.

Yanovskaya, T.B., Antonova, L.M., and Kozhevnikov, V.M., 2000. Lateral variations of the upper mantle structure in Eurasia from group velocities of surface waves, *Phys. Earth Planet. Inter*., **122**, 19-32.

Yao, H., R.D. van der Hilst, and M. V. de Hoop, 2006. Surface-wave tomography in SE Tibet from ambient seismic noise and two-station analysis: I. – Phase velocity maps, *Geophys. J. Int*., submitted.

Yoshizawa, K. & Kennett, B. L. H., 2002. Determination of the influence zone for surface wave paths, *Geophys. J. Int.*, **149**,440-453.

Zhou Y., Dahlen, F.A. & Nolet, G., 2004. 3-D sensitivity kernels for surface-wave observables, *Geophys. J. Int.*, **158**, 142-168.

Figure captions:

Figure 1. Broad-band seismic stations in Europe used in this study, marked by red triangles.

Figure 2. Example of a 12-month broad-band symmetric-component cross-correlation between the station-pair IBBN (Ibbenbueren, Germany) and TIRR (Hungary). The red line shows the great-circle linking the two stations. The broad-band cross-correlation is filtered into five sub-bands. Note the clear normal dispersion of the Rayleigh waves, with the longer periods arriving earlier.

Figure 3. Example of a 12-month symmetric-component cross-correlation record-section

centered on the station TUE (Stuetta, Italy) and band-pass filtered from 20 – 50 sec period. Only cross-correlations with SNR > 7 are shown at right with the corresponding paths delineated by red lines at left. The diagonal gray line indicates the approximate arrival time for Rayleigh waves in this band.

Figure 4. Example of dispersion measurement. (Top) One-year cross-correlation obtained between stations IBBN (Ibbenbueren, Germany) and TUE (Stuetta, Italy), which are separated by 650 km. (Middle) Raw frequency-time (FTAN) diagram in which the thick line is the raw dispersion measurement. (Bottom) Cleaned FTAN diagram obtained after applying the phase-matched filter based on the raw dispersion measurement. The thin lines in the Middle and Bottom panels are the dispersion curve predicted from the global 3-D shear velocity model (Shapiro and Ritzwoller, 2002).

Figure 5. **(a)** Number of measurements versus signal-to-noise ratio from the 12-month stacked cross-correlations. (b) Number of measurements remaining after several steps in data reduction. (c) Average path length of the accepted dispersion measurements. (d) Average group speed uncertainties versus period. (e) Average travel time uncertainties versus period.

Figure 6. An example of seasonal variability of the dispersion measurements. (Top) The path considered is between stations HGN (Heijmans Groeve, Netherlands) and PSZ (Piszkes-teto, Hungary). (Bottom) The red curves are group velocity measurements obtained on twelve 3-month cross-correlations band-pass filtered from 8 to 50 sec period. The black line is the prediction from the global 3-D model (Shapiro and Ritzwoller, 2002).

Figure 7. Histograms of misfit for ambient noise data (left) and earthquake data (right) at

16 sec period. Misfit is calculated from the corresponding over-smooth tomographic map inverted from ambient noise data and earthquake data. Ambient noise data are taken prior to the stage where measurements are rejected due to large misfit. The standard deviation is shown at the left top of each diagram.

Figure 8. Path density (left column) and resolution estimates (right column) at 16 sec period. Path density is defined as the number of rays intersecting a $1^0 \times 1^0$ (111 km x 111 km) square cell. Resolution is presented in units of km, and is defined as the standard deviation of a 2-D Gaussian fit to the resolution surface at each model node.

Figure 9. Estimated group speed maps at 10, 20, 30, and 40 sec periods. Maps are presented as a perturbation from the average across the map in percent.

Figure 10. Group speed maps at 16 sec period. (a) Estimated group speed map determined with a reference map. (b) Difference between the estimated map in (a) and the reference map presented in Fig. 12a. (c) Estimated group speed map determined without a reference map. (d) Difference between the two estimated maps in (a) and (c).

Figure 11. Same as Fig. 10, but for 35 sec period. The reference map used is presented in Fig. 12b.

Figure 12. Reference maps computed from the 3-D model of Shapiro and Ritzwoller (2002) at (a) 16 sec and (b) 35 sec period.

Figure 13. Various misfit statistics for the estimated group speed maps to the observations taken after all stages of data rejection are complete. (Top) Misfit is represented as reduction of variance delivered by (solid line) the estimated maps relative

to the predicted group velocity maps from the global 3-D model (Shapiro and Ritzwoller, 2002) and (dashed line) the average velocity across each map. (Middle) RMS group velocity misfit presented versus period. (Bottom) RMS travel time misfit presented versus period.

Figure 14. Standard deviations of data misfit after tomography with an over-smoothed model, presented as a function of period for ambient noise data (solid line) and earthquake data (dashed line). In contrast with Figure 13c and similar to Figure 7, the last stage of data rejection has not been applied here.

Figure 15. Maps of sediment thickness (left) and crustal thickness (right). Sediment thicknesses are taken from CRUST1.0, which Laske and Masters digitized across most of Europe from the EXXON Tectonic Map of the world. Crustal thicknesses are taken from CRUST2.0. The locations of geological units discussed in the text are marked approximately.

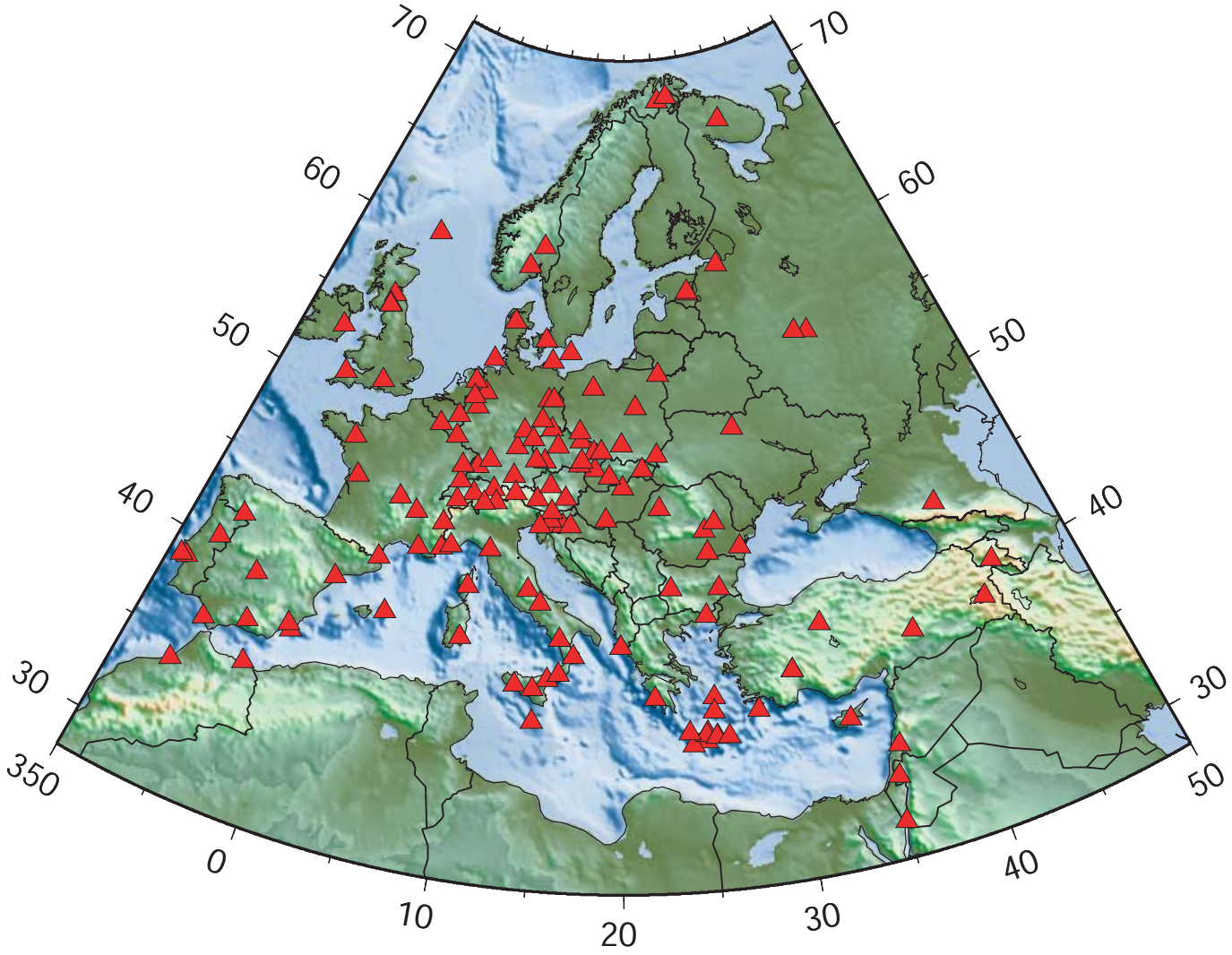
70
60
50
40
30
350
0
10
20
30
40
50

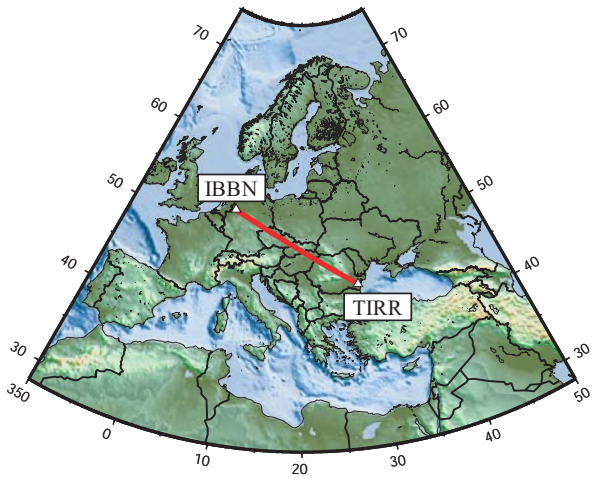
IBBN
TIRR
70
60
50
40
30
350
0
10
20
30
40
50

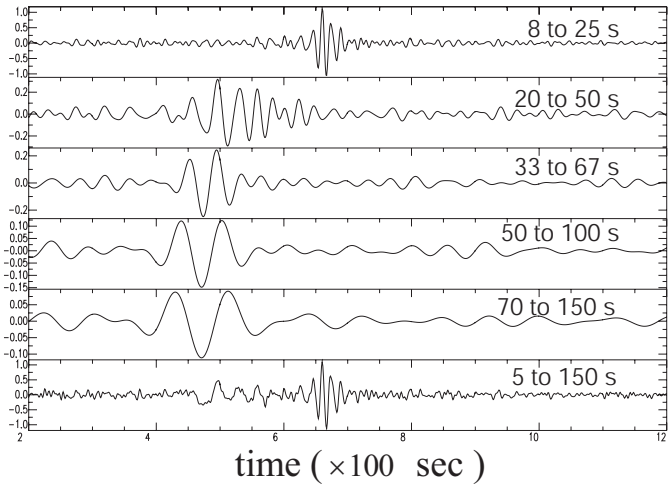
8 to 25 s
20 to 50 s
33 to 67 s
50 to 100 s
70 to 150 s
5 to 150 s
time (×100 sec)

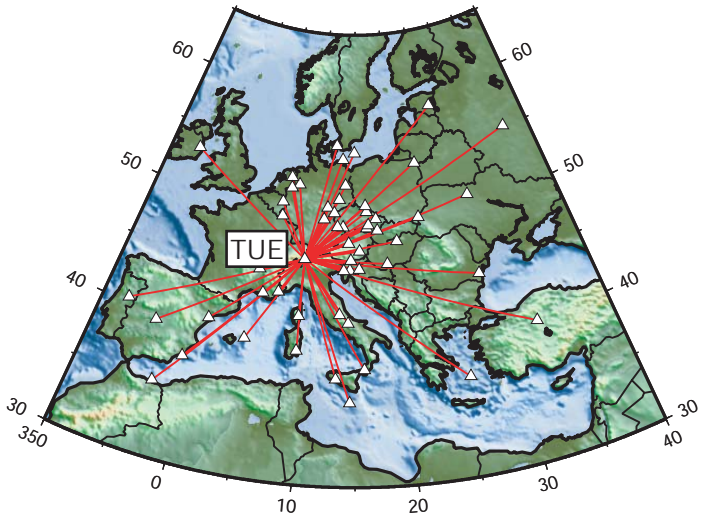
TUE
60
50
40
30
350
0
10
20
30
40

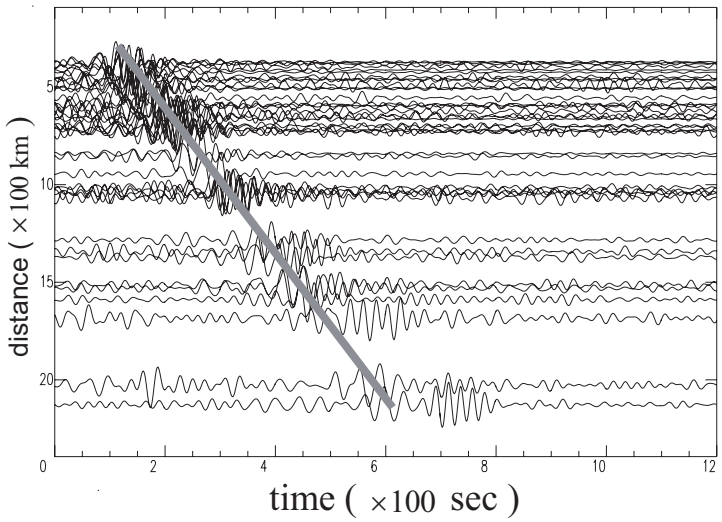
distance (×100 km)
time (×100 sec)
0
2
4
6
8
10
12
5
10
15
20

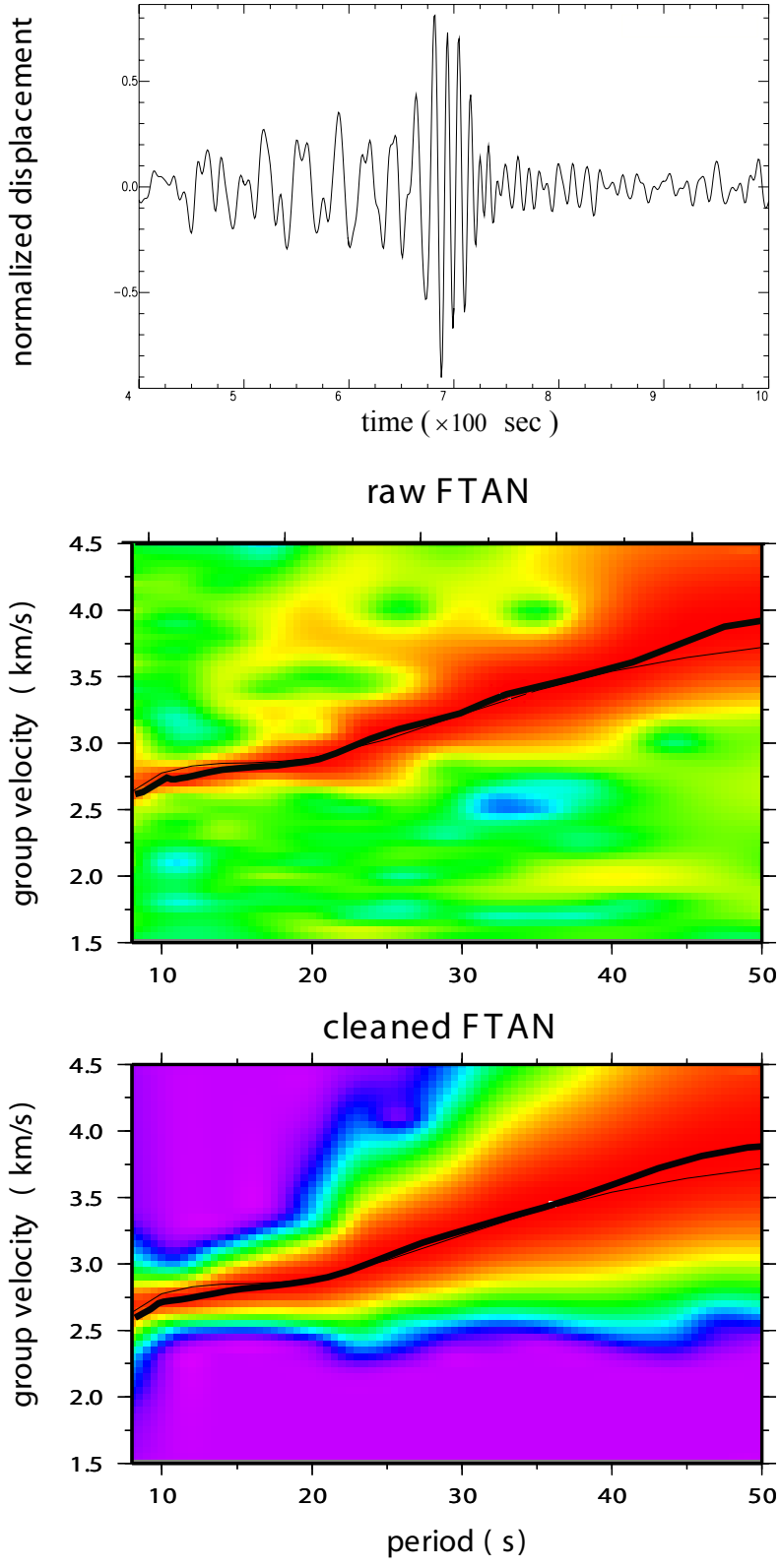
normalized displacement
0.5
0.0
−0.5
4
5
6
7
8
9
10
time (×100 sec)
raw FTAN
group velocity (km/s)
4.5
4.0
3.5
3.0
2.5
2.0
1.5
10
20
30
40
50
cleaned FTAN
group velocity (km/s)
4.5
4.0
3.5
3.0
2.5
2.0
1.5
10
20
30
40
50
period (s)

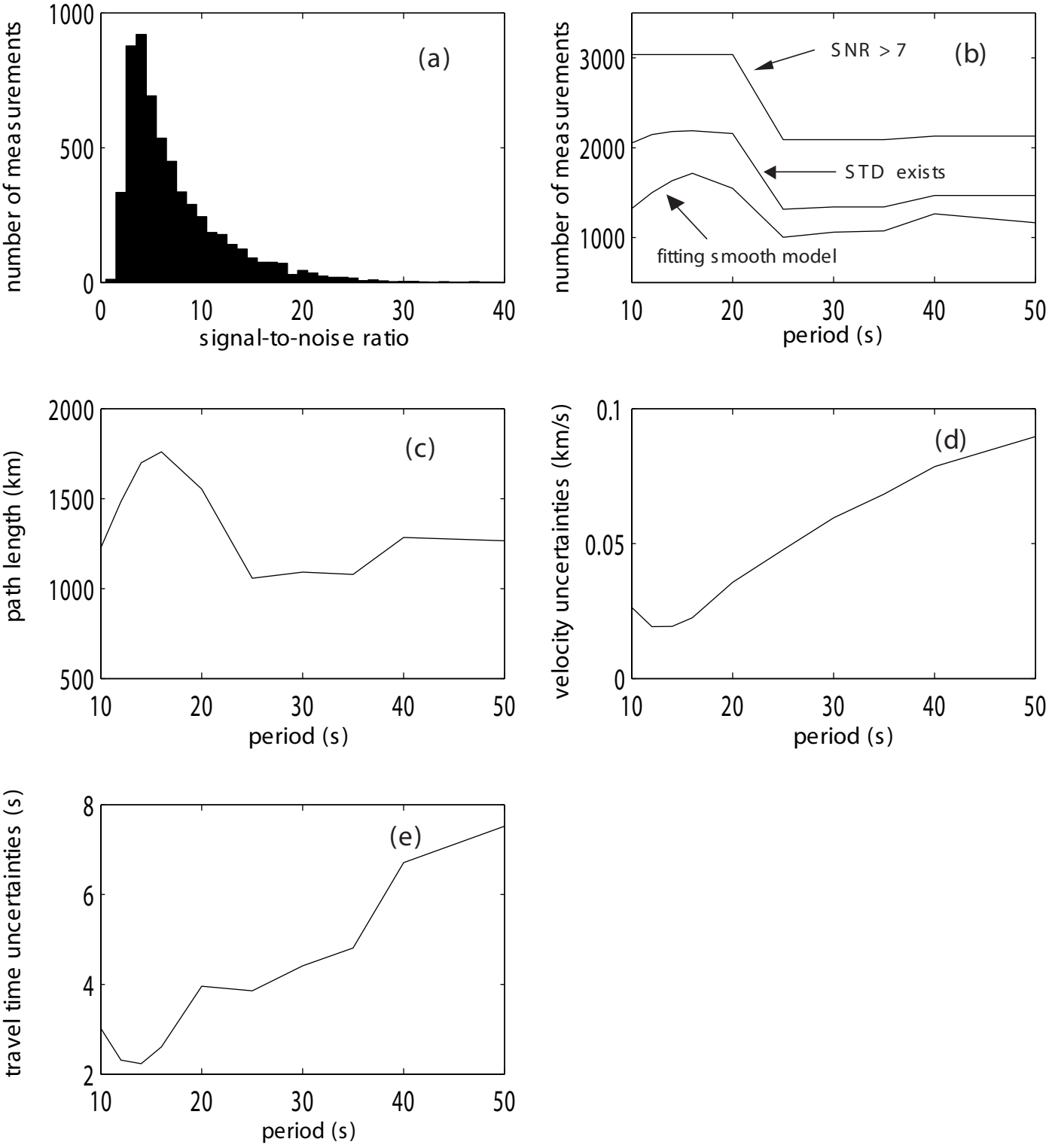
(a)
number of measurements
signal-to-noise ratio
1000
500
0
0
10
20
30
40
(b)
SNR > 7
STD exists
fitting smooth model
number of measurements
period (s)
3000
2000
1000
10
20
30
40
50
(c)
path length (km)
period (s)
2000
1500
1000
500
(d)
velocity uncertainties (km/s)
period (s)
0.1
0.05
0
(e)
travel time uncertainties (s)
period (s)
8
6
4
2

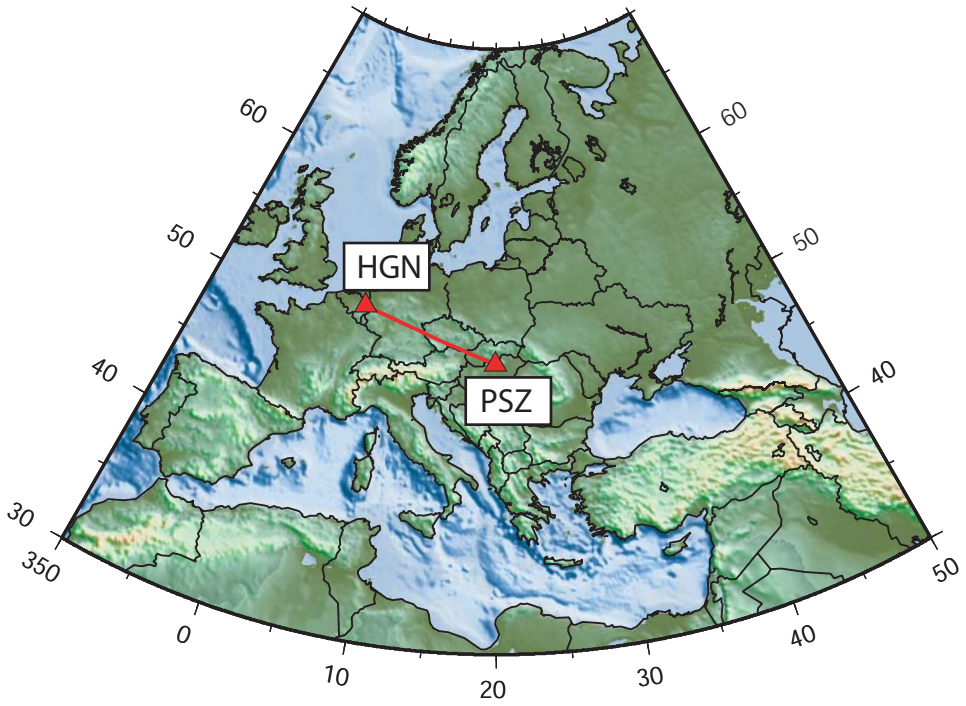
HGN
PSZ
60
50
40
30
350
0
10
20
30
40
50

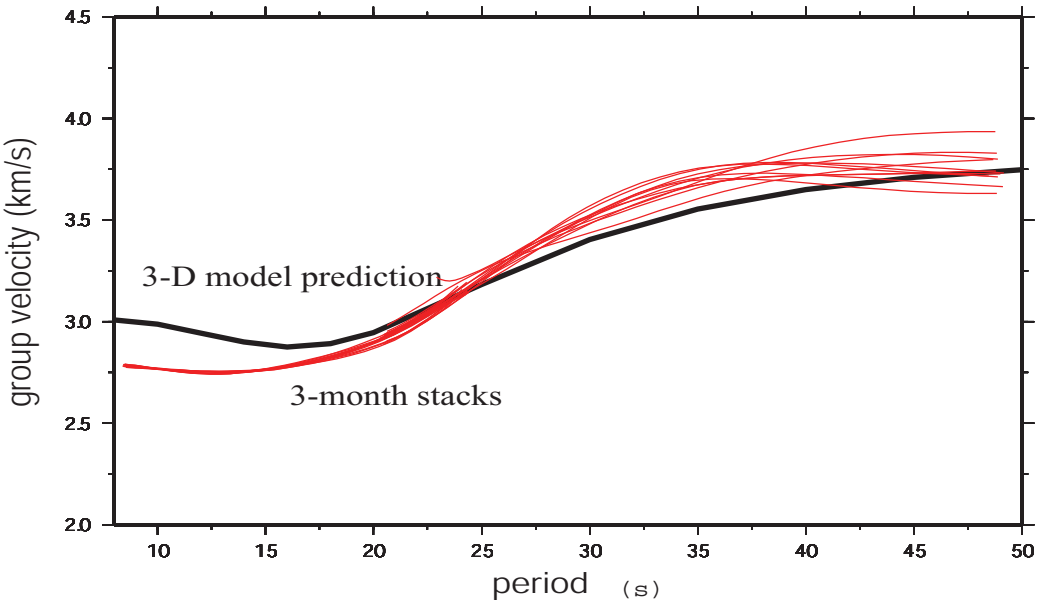
group velocity (km/s)
period (s)
3-D model prediction
3-month stacks
4.5
4.0
3.5
3.0
2.5
2.0
10
15
20
25
30
35
40
45
50

misfit to ambient noise measurements: 16 sec

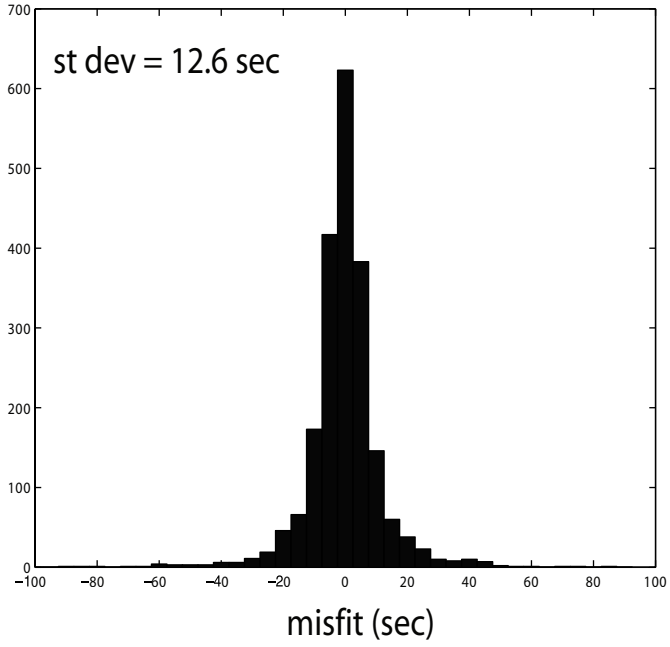

misfit to earthquake measurements: 16 sec

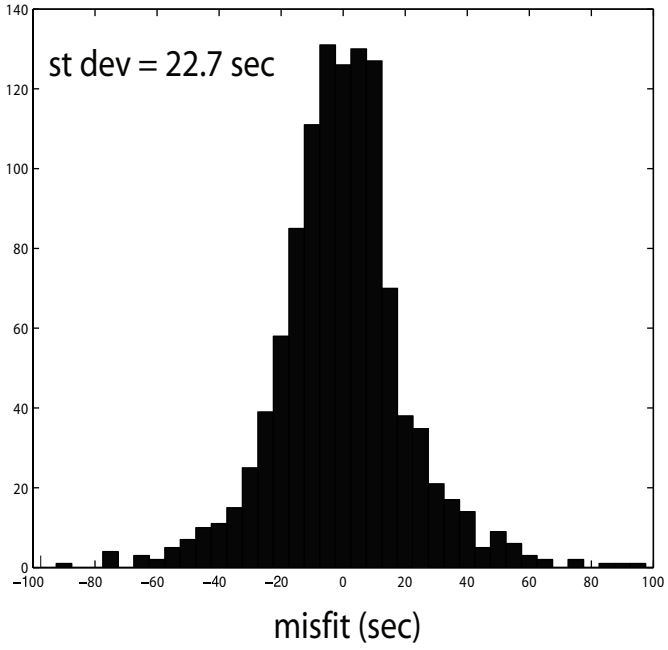

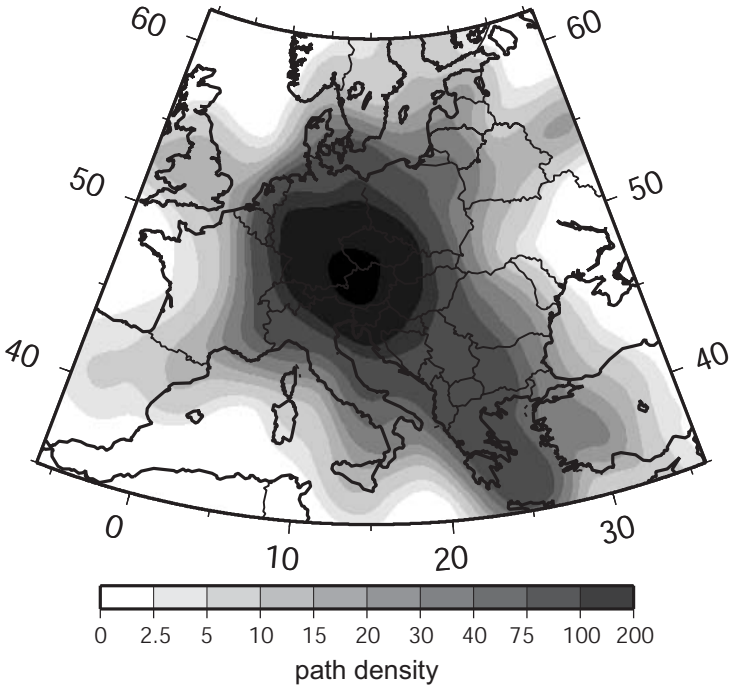
60
50
40
0
10
20
30
0 2.5 5 10 15 20 30 40 75 100 200
path density

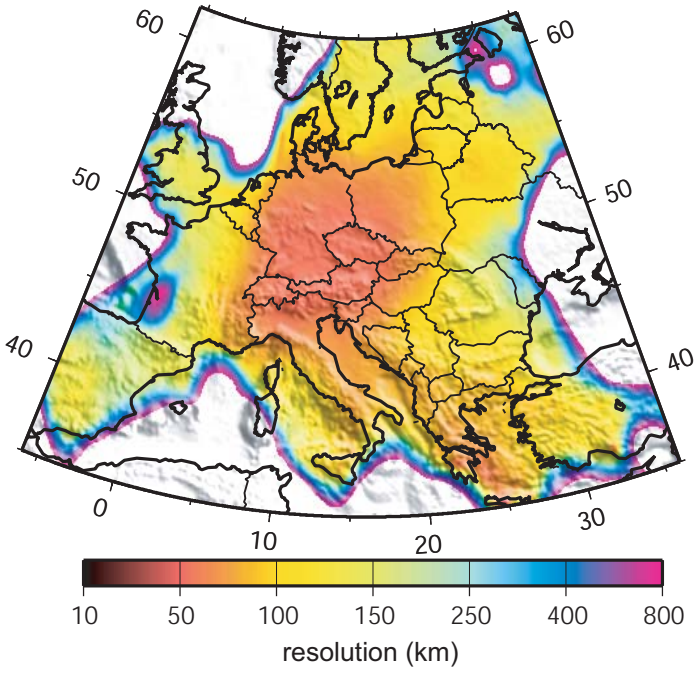
60
50
40
0
10
20
30
10 50 100 150 250 400 800
resolution (km)

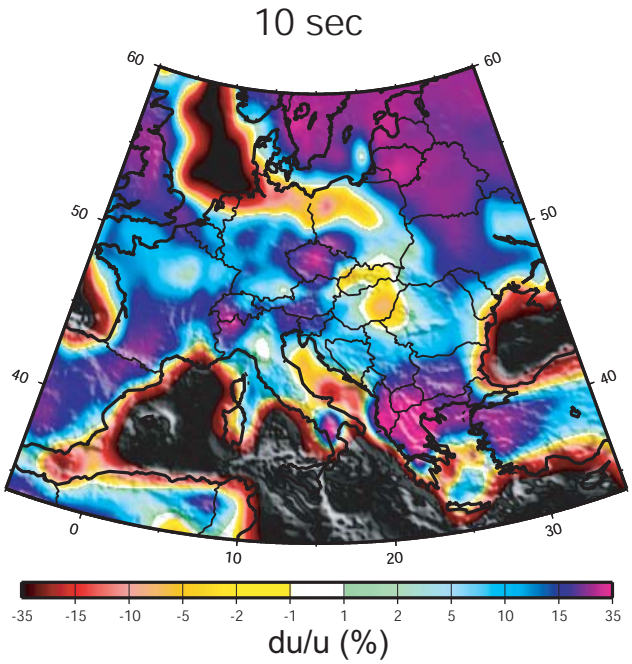
10 sec
60
50
40
0
10
20
30
-35 -15 -10 -5 -2 -1 1 2 5 10 15 35
du/u (%)

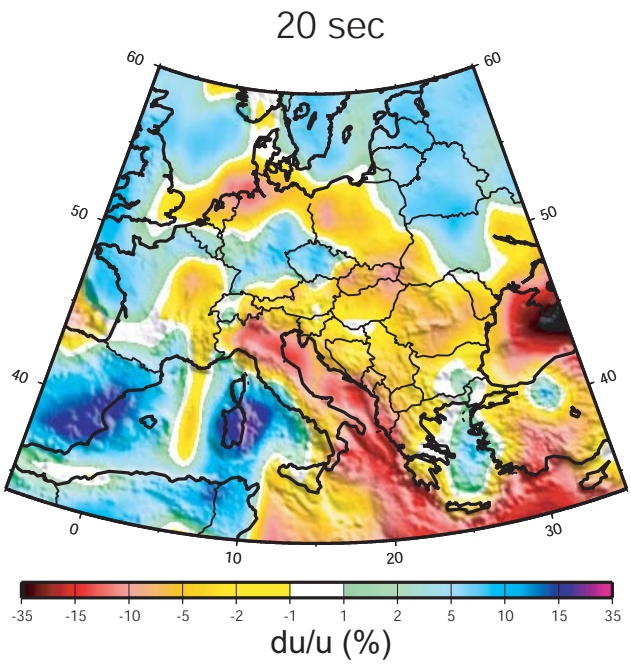
20 sec
60
50
40
0
10
20
30
-35 -15 -10 -5 -2 -1 1 2 5 10 15 35
du/u (%)

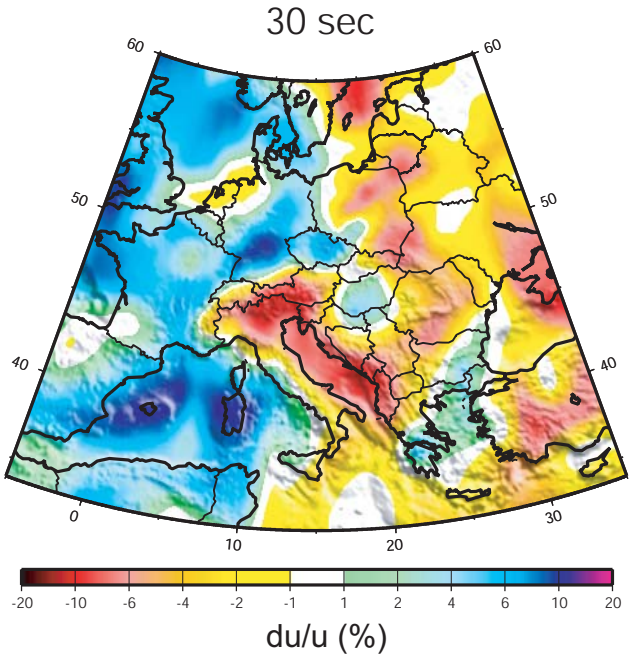
30 sec
60
50
40
0
10
20
30
-20 -10 -6 -4 -2 -1 1 2 4 6 10 20
du/u (%)

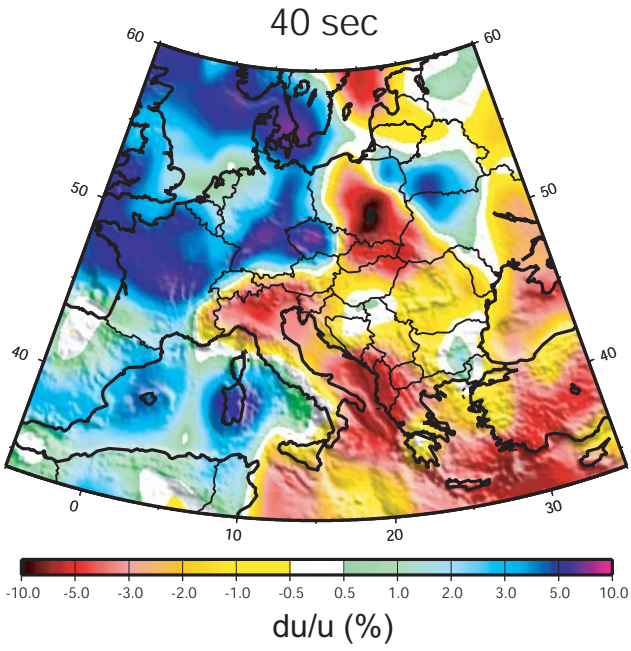
40 sec
60
50
40
0
10
20
30
-10.0 -5.0 -3.0 -2.0 -1.0 -0.5 0.5 1.0 2.0 3.0 5.0 10.0
du/u (%)

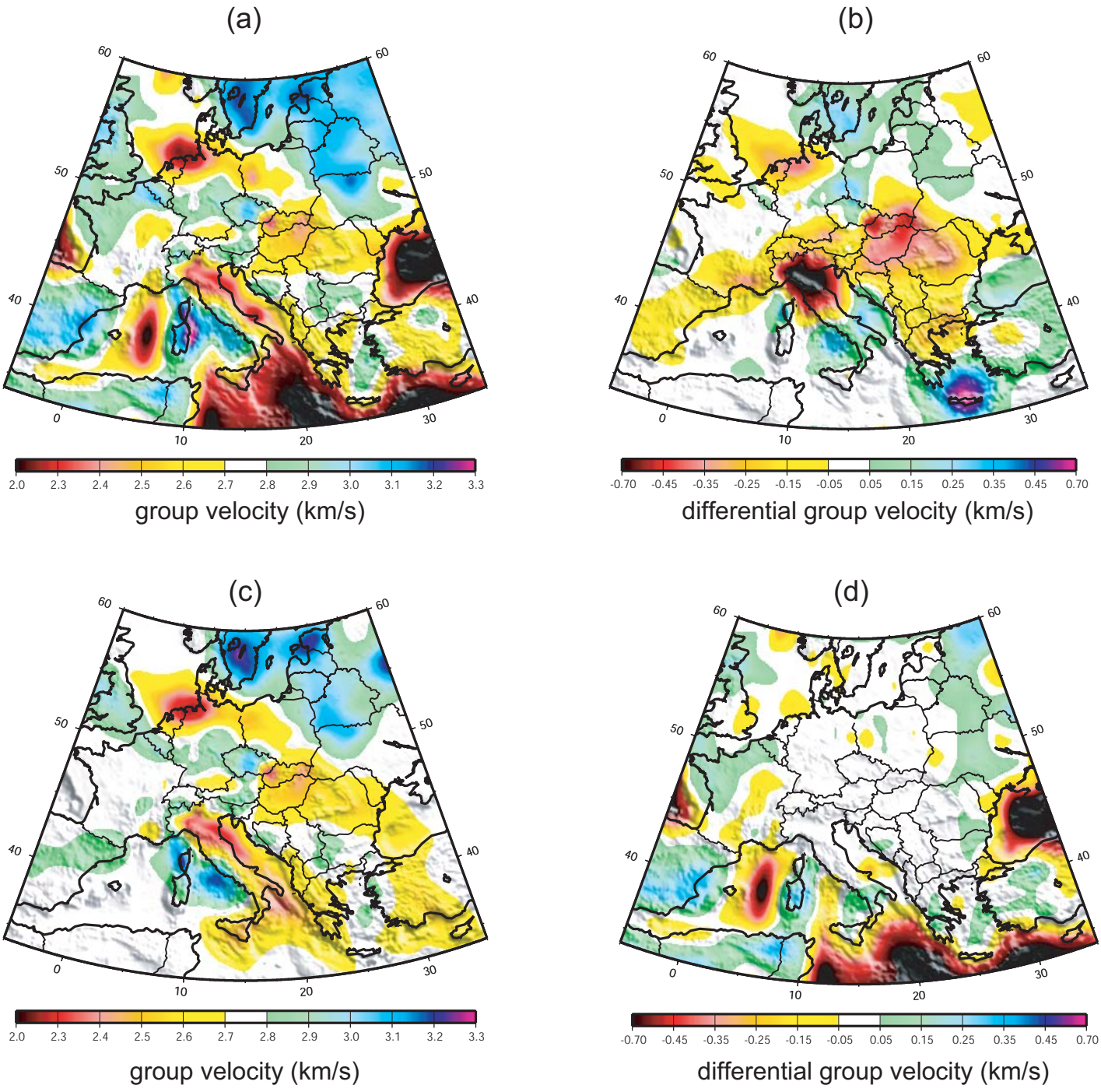
(a)
(b)
(c)
(d)
60
50
40
0
10
20
30
2.0 2.3 2.4 2.5 2.6 2.7 2.8 2.9 3.0 3.1 3.2 3.3
group velocity (km/s)
-0.70 -0.45 -0.35 -0.25 -0.15 -0.05 0.05 0.15 0.25 0.35 0.45 0.70
differential group velocity (km/s)

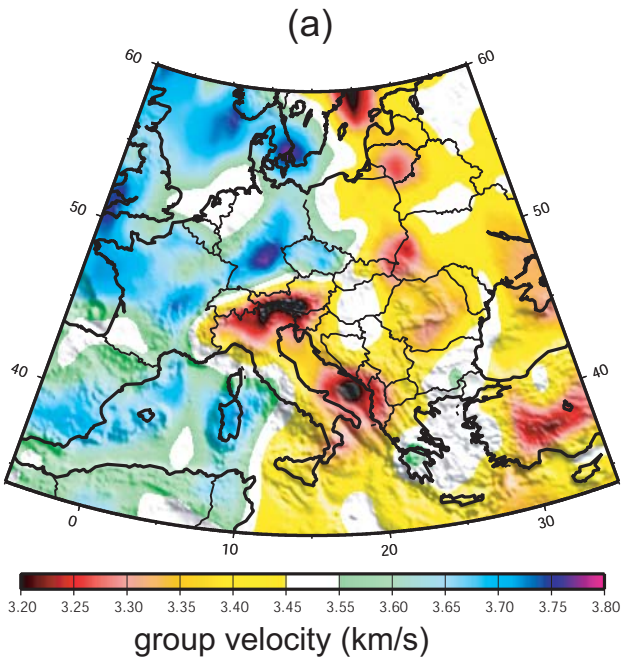
(a)
60
50
40
0
10
20
30
3.20 3.25 3.30 3.35 3.40 3.45 3.55 3.60 3.65 3.70 3.75 3.80
group velocity (km/s)

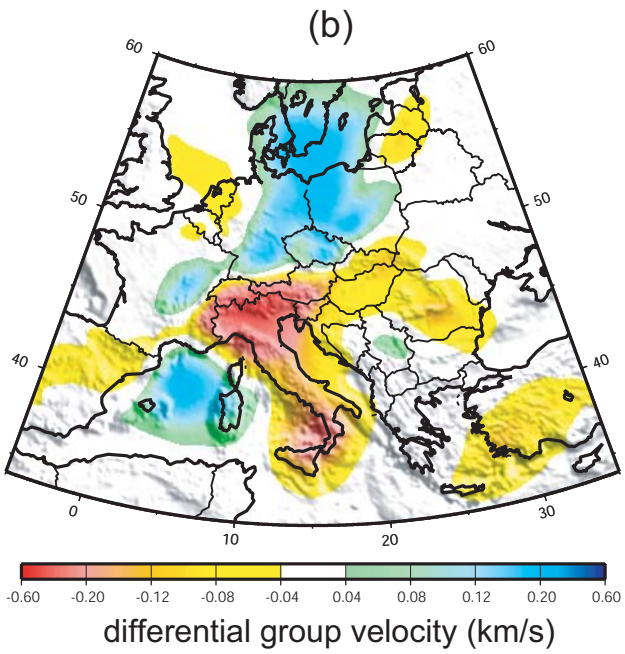
(b)
-0.60 -0.20 -0.12 -0.08 -0.04 0.04 0.08 0.12 0.20 0.60
differential group velocity (km/s)

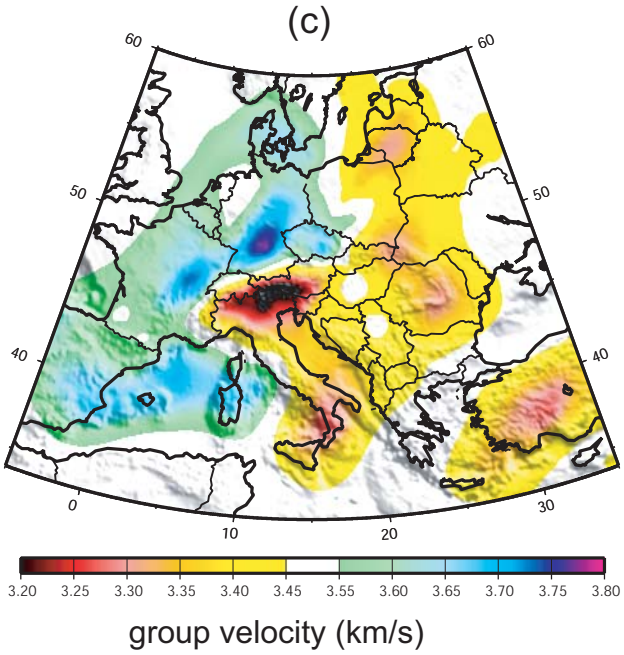
(c)
3.20 3.25 3.30 3.35 3.40 3.45 3.55 3.60 3.65 3.70 3.75 3.80
group velocity (km/s)

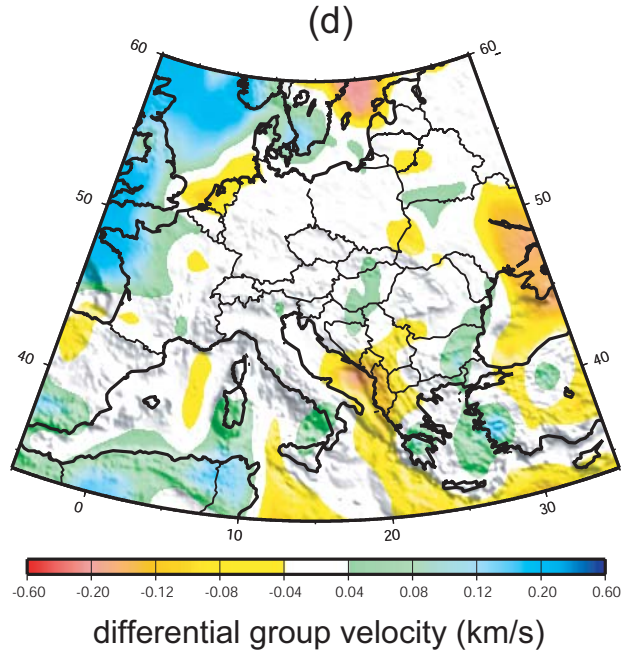
(d)
-0.60 -0.20 -0.12 -0.08 -0.04 0.04 0.08 0.12 0.20 0.60
differential group velocity (km/s)

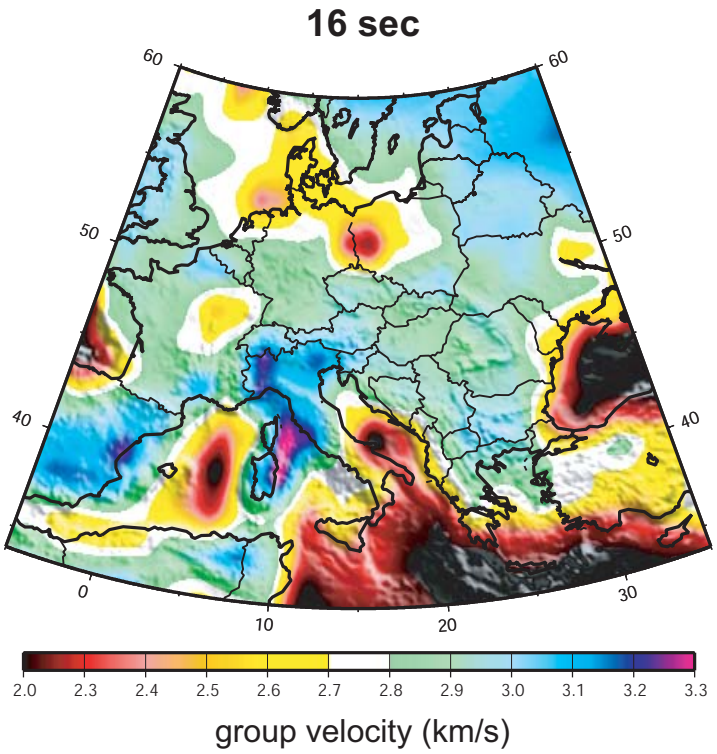
16 sec
60
50
40
0
10
20
30
2.0
2.3
2.4
2.5
2.6
2.7
2.8
2.9
3.0
3.1
3.2
3.3
group velocity (km/s)

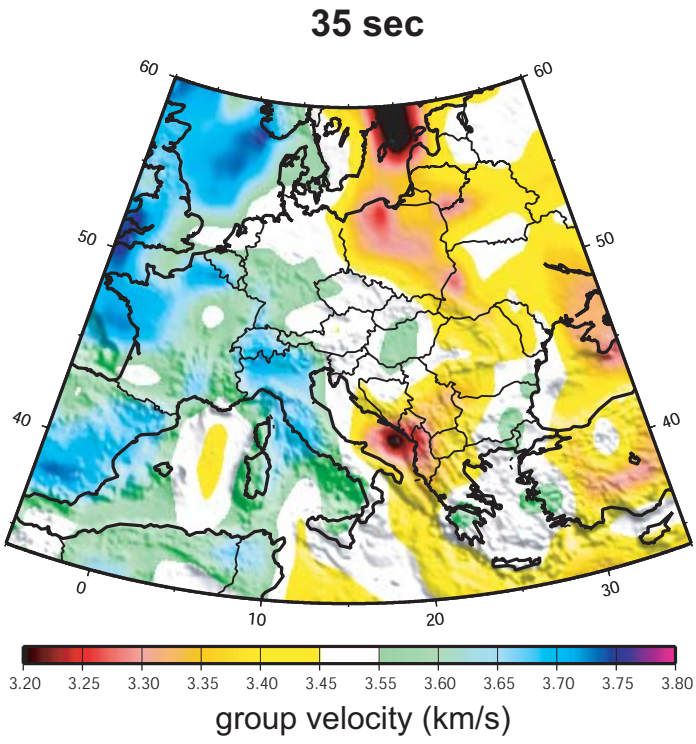
35 sec
60
50
40
0
10
20
30
3.20
3.25
3.30
3.35
3.40
3.45
3.55
3.60
3.65
3.70
3.75
3.80
group velocity (km/s)

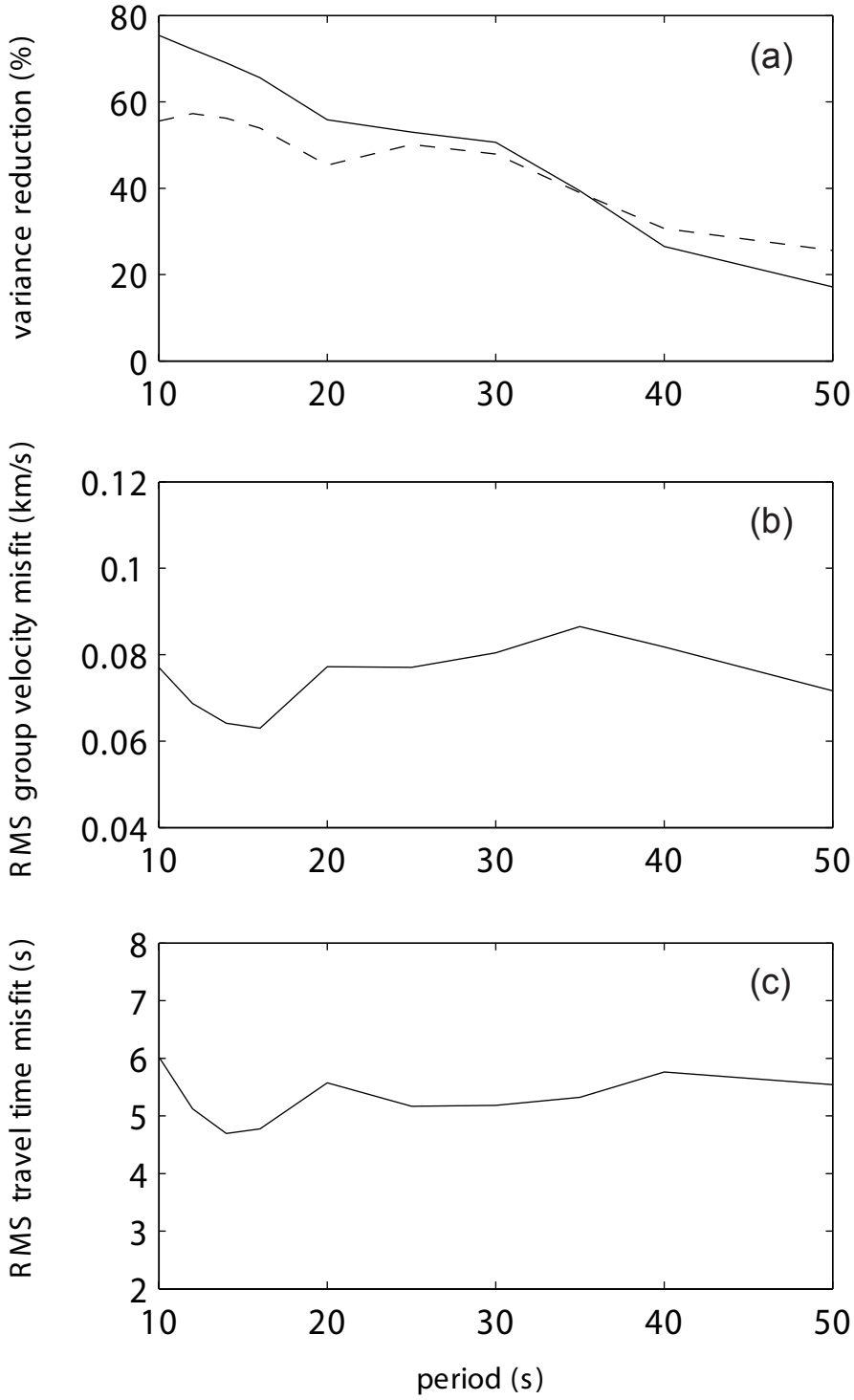
variance reduction (%)
80
60
40
20
0
10
20
30
40
50
(a)
RMS group velocity misfit (km/s)
0.12
0.1
0.08
0.06
0.04
(b)
RMS travel time misfit (s)
8
7
6
5
4
3
2
(c)
period (s)

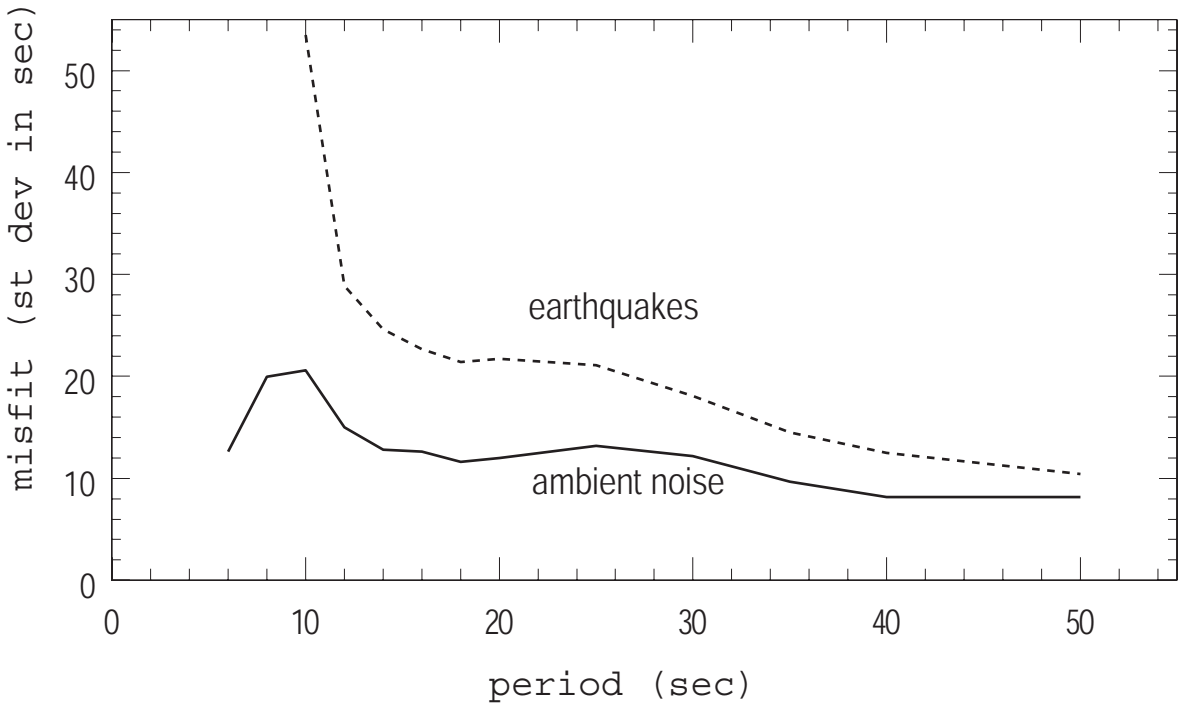
misfit (st dev in sec)
0
10
20
30
40
50
earthquakes
ambient noise
0
10
20
30
40
50
period (sec)

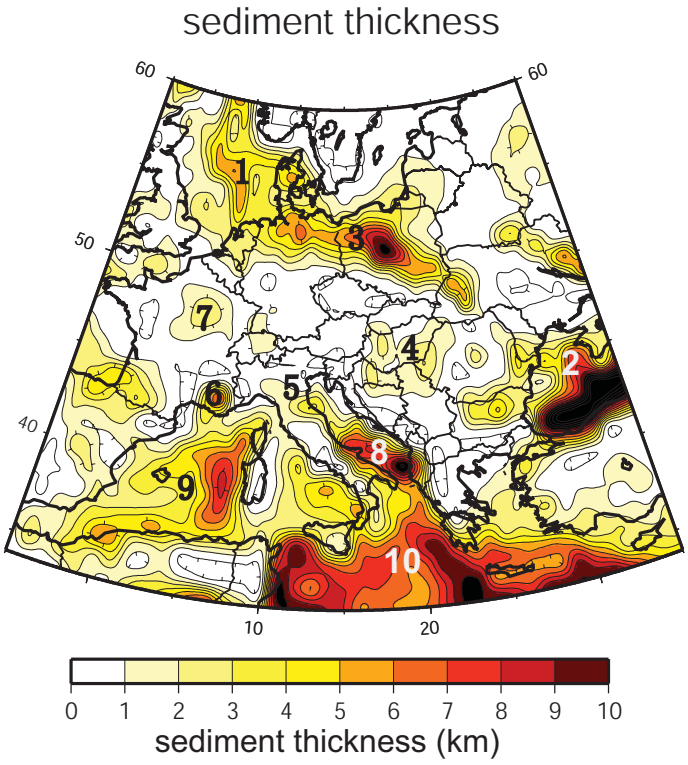

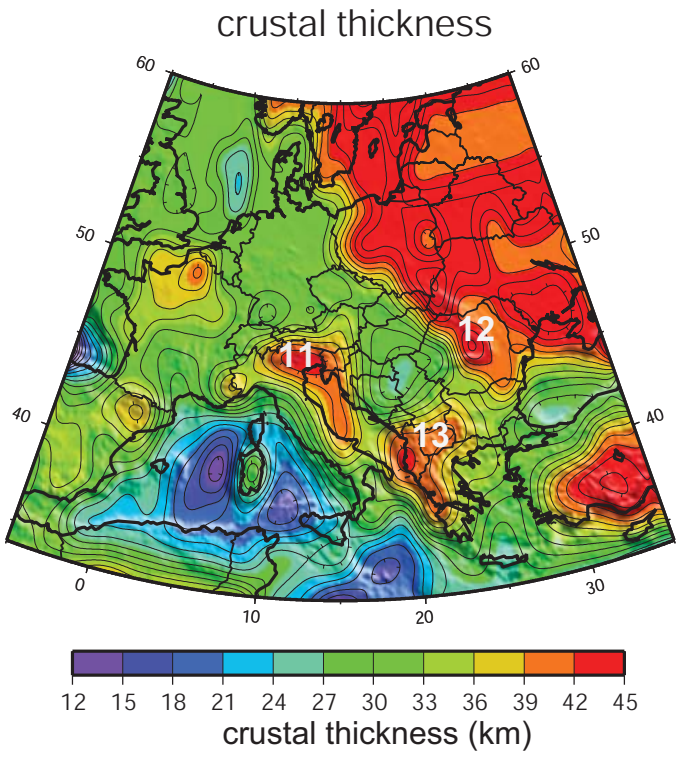

1. North Sea
2. Black Sea
3. Silesian Basin
4. Pannonian Basin
5. Po Basin
6. Rhone Basin
7. Paris Basin
8. Adriatic Sea
9. W. Mediterranean
10. E. Mediterranean
11. Alps
12. Carpathians
13. Balkan